Bachelor Thesis

Analysis of Flux Distributions of the Blazars Mrk 421 and Mrk 501 in Very High Energies

Laura Eisenberger

Würzburg, March 2021

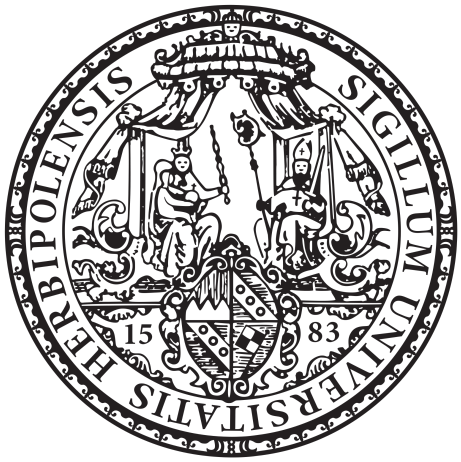

Julius-Maximilians-Universität Würzburg
Faculty of Physics and Astronomy

Supervisor: Prof. Dr. Karl Mannheim

Abstract

Blazars dominate the extragalactic sky at very high energies. As one type of Active Galactic Nuclei (AGN), extremely luminous compact zones at the center of galaxies powered by accretion onto supermassive black holes, they are characterised by the pointing of their relativistic jet into the observer's direction. However, the physical mechanisms responsible for their variable, highly energetic emission are still unclear. A possible scenario is that particles are accelerated at shock waves propagating along the jet [1]. Relativistic beaming effects could explain the variability of the gamma-ray emission produced by the fastest electrons. From flux distributions of blazars, active and steady emission states could become apparent. Whether one can extrapolate physical mechanisms from the shape of flux distributions is discussed controversially. Normal and log-normal flux distributions are commonly associated with additive and multiplicative processes respectively. However, Scargle proved in his enquiry 2020 that log-normalcy can not rule out additive models [2]. Ground-based telescopes such as FACT can measure indirectly very-high-energy fluxes by means of detection of Cherenkov light from gamma-ray induced air showers. Since the Crab Nebula is stable at TeV energies, it serves as a calibration source to correct the light curves for observational effects and to convert the measured gamma rates into fluxes. The detection systematics of the instrument is quantified by the flux distribution of the non-detected source 1H0323+342. For the blazars Markarian 421 (Mrk 421) and Markarian 501 (Mrk 501), the brightest known sources at TeV energies, FACT provides data acquired from 2012 to 2019 during 786 nights (1882 hours in total) and 896 nights (1725 hours in total) respectively.

The nightly fluxes of both sources are investigated with respect to the underlying shape of their distributions. For equal histogram bins as wide as the mean error of the fluxes, the superposition of normal and log-normal components is suitable to describe the data which is not the case for Bayesian bins representing the observed distribution with its significant features as well as possible. For the latter, the flux distributions are rather log-normal or at least positively skewed indicating flaring behaviour during active phases. Apart from that, it is demonstrated that the larger the time binning of the light curves is, the smaller the mean error, the total number of histogram entries and the flux range. It is shown that the temporal evolution of Mrk 501 from an active to a low state is reflected in its flux distributions by the transition from a log-normal to a normal one. The comparison of both sources reveals that over the observed period of eight years Mrk 501 has the lower ground state, whereas Mrk 421 is more variable. The upper limits for the baseline flux are determined to be 4% of the flux of the Crab Nebula at TeV energies for Mrk 501 and 35% for Mrk 421, which is compared to previous results of [3] and [4].

Zusammenfassung

Blazare dominieren den extragalaktischen Raum im Bereich der höchsten Energien und gehören zu den aktiven Galaxienkernen, extrem leuchtkräftigen Kernregionen von Galaxien angetrieben durch Akkretion von Materie auf supermassive schwarze Löcher. Blazare zeichnen sich im Speziellen durch die Orientierung ihres relativistischen Jets in Richtung des Beobachters aus und emittieren hochenergetische, in ihrer Intensität variable Strahlung, wobei bisher ungeklärt ist, welche physikalischen Mechanismen deren Entstehung zugrundeliegen. Ein mögliches Szenario ist die Beschleunigung von Teilchen durch Schockwellen, die sich entlang des Jets ausbreiten [1]. Relativistische Beaming-Effekte könnten die Variabilität der von den energiereichsten Elektronen emittierte Gamma-Strahlung erklären. Aus den Flussverteilungen von Blazaren werden möglicherweise Grund- bzw. aktive Zustände deutlich. Ob nur aus der Form der Verteilung direkt auf physikalische Mechanismen geschlossen werden kann, wird kontrovers diskutiert. Normale und lognormale Flussverteilungen werden zumeist mit additiven bzw. multiplikativen Prozessen in Verbindung gebracht, wohingegen Scargle in seiner Untersuchung 2020 zeigt, dass Lognormalität additive Modelle nicht ausschließt [2].
Terrestrische Teleskope wie FACT messen hochenergetische Flüsse auf indirekte Weise durch die Detektion von Cherenkov-Strahlung, welche in durch Gammastrahlen in der Erdatmosphäre induzierten Teilchenschauern auftritt. Der Krebsnebel dient dabei als Kalibrierungsquelle für die Korrektur der Lichtkurven hinsichtlich beobachtungsbedingten Einflüssen und für die Umrechnung der gemessenen Gamma-Raten in Flüsse. Die Detektorsystematik wird durch die Flussverteilung der nicht detektierte Quelle 1H0323+342 quantifiziert. Für die hellsten der bekannten Quellen im TeV-Energiebereich, die Blazare Markarian 421 (Mrk 421) and Markarian 501 (Mrk 501), stehen FACT-Daten von 2012 bis 2019 aus 786 bzw. 896 Nächten (insgesamt 1882 bzw. 1725 Stunden) zur Verfügung.
Die nächtlichen Flüsse der beiden Quellen werden hinsichtlich der zugrundeliegenden Form ihrer Verteilungen untersucht. Für eine gleichmäßige Klassengröße im Histogramm entsprechend dem durchschnittlichen Fehler der Flüsse erweist sich die Superposition einer Normal- und Lognormalkomponente am geeignetsten, was jedoch für das sogenannte Bayesian Binning nicht der Fall ist. Dabei erfolgt eine an die Daten angepasste Klasseneinteilung, die eine optimale Beschreibung der Daten ermöglicht. Demnach sind die Verteilungen entweder von lognormaler Natur oder weisen zumindest eine positive Schiefe auf, was auf Strahlungsausbrüche während aktiver Phasen hindeutet. Außerdem wird deutlich, dass mit größerem zeitlichen Binning der Flüsse der durchschnittliche Fehler, die Gesamtzahl der Einträge im Histogramm und der Wertebereich des Flusses abnimmt.

Schließlich wird gezeigt, dass sich für Mrk 501 die zeitliche Entwicklung vom Aktiv- in den Ruhezustand durch einen Übergang von lognormal zu normal in den Flussverteilungen widerspiegelt. Der Vergleich der beiden Quellen lässt erkennen, dass Mrk 501 über den beobachteten Zeitraum von acht Jahren einen niedrigeren Grundzustand besitzt, während Mrk 421 die variablere Quelle ist. Als obere Grenze des Grundzustands ergibt sich für Mrk 501 4% und für Mrk 421 35% des Flusses des Krebsnebels bei TeV Energien, was mit den Ergebnissen aus [3] und [4] verglichen wird.

Contents

1. Introduction **1**

1.1. AGN Phenomenon 1

1.1.1. Classification 2

1.1.2. Unification Scheme 3

1.2. Very-High-Energy Astronomy 5

1.2.1. Imaging Atmospheric Cherenkov Telescopes (IACTs) 6

1.3. Blazar Emission Models 10

1.3.1. Production of Gamma Radiation 10

1.3.2. Relativistic Beaming 12

1.3.3. Variability and Flux States 13

2. Investigation of Flux Distributions **14**

2.1. Interpretation of Flux Distributions 14

2.1.1. Normal Distribution 14

2.1.2. Log-Normal Distribution 15

2.2. Properties of FACT Data 17

2.2.1. Observational Effects 17

2.2.2. Detector Systematics 18

2.2.3. Sample and Data Selection 19

2.3. Method 21

2.3.1. Statistical Considerations 21

2.3.2. Bayesian Binning 22

2.3.3. Fit Functions 23

2.4. Results Mrk 421 24

2.4.1. Regular Binning 24

2.4.2. Different Time Binnings 27

2.4.3. Bayesian Binning 27

2.5. Results Mrk 501 30

2.5.1. Binning Effects 30

2.5.2. Temporal Evolution 30

2.6. Comparison of Mrk 421 and Mrk 501 35

3. Conclusion **37**

Bibliography **39**

A. Appendix **40**

A.1. Overview of Fit Parameters 40

A.2. Implementation of the chi-squared Test in Python 43

1. Introduction

Before investigating the flux distributions of the blazars Markarian 421 (Mrk 421) and Markarian 501 (Mrk 501), an introduction to the physical background of Active Galactic Nuclei (AGN) and the Very-High-Energy (VHE) astronomy is given. Most information in this chapter is inspired by Beckmann's and Shrader's textbook [5] which provides a very useful overview on the current knowledge of the AGN phenomenon. Details about the atmospheric Cherenkov technique are taken from Weekes's textbook "Very High Energy Gamma-Ray Astronomy" [6].

1.1. AGN Phenomenon

Active Galactic Nuclei are extremely luminous, but fairly compact and cosmologically distant objects in the Universe. They are powered by accretion onto black holes with masses exceeding that of the sun a million times. Such supermassive black holes are assumed to be located at the center of most galaxies, but not all of them appear as AGN. Persistent energetic behaviour only occurs whenever there is enough supply of material within a critical distance around the central engine so that radiatively efficient accretion is possible. The emitted radiation through accretion has a thermal origin. Due to the gravitational field of the black hole, the surrounding material is drawn inwards and thereby strongly heated.

However, one has to deal with various radiative processes in order to understand the observed AGN spectra. Synchrotron radiation plays an important role in the radio domain. Scattering of photons complicates the interpretation of emission spectra because the photons lose or gain energy on their way to the observer through interaction with particles. In fact, the highest photon energies are reached through inverse Compton scattering where photons gain energy from highly relativistic electrons.

The interaction of charged particles with magnetic fields can lead to collimation of matter from each face of the accretion disk. The formation of such jets along the axis of rotation is a complex and still not completely understood phenomenon. As we will see in the following section, the occurrence of a jet and its orientation with respect to the observer's line of sight define among other parameters the identification of different AGN classes.

1.1.1. Classification

The different appearances of the AGN phenomenon and the history of its discovery led to classification into various subclasses. Historically, Seyfert galaxies were the first objects identified as AGN and still count as the most common AGN type. With the advent of large-scale radio observations, one discovered distant radio sources which appeared like blue stars in optical images and were therefore named quasi-stellar radio sources, or quasars. Soon it was noticed that quasars are actually the same phenomena as Seyfert galaxies but at further distances. For this reason, quasars are now differentiated from Seyfert objects according to their brighter absolute magnitude. This shows that the AGN classification is often ambiguous, and besides, not always the same in different ranges of the electromagnetic spectrum. Over time, more and more types and subclasses arised with the discovery of numerous AGN-like sources in many different wavelengths.
In general, one distinguishes between radio-loud and radio-quiet AGN although it is likely that the transition is continuous. The radio loudness is measured by the radio to optical flux ratio and is associated with beamed emission.
The radio-quiet Seyfert galaxies do not produce jets and show highly ionized emission lines from their central core. Based on this spectral signature in the optical regime, one further distinguishes between Seyfert class 1 and Seyfert class 2. Seyfert 1 spectra are characterised by broad Balmer and narrow forbidden lines, in contrast to Seyfert 2 galaxies which show only narrow lines. The Doppler broadening of the permitted lines indicates high velocities and high-density gas and thereby presents an unobscured view of the nucleus. If the lines are of narrow width, the amount of absorbing dust is believed to be much higher and therefore the central core emission appears less dominant.
In the radio-loud regime, one can make the broad division into the Fanaroff-Riley class I (FR-I) and class II (FR-II) and the highly variable, gamma-ray emitting blazars.
The low-luminosity FR-I sources have a jet-dominated radio structure, whereas the emission of the high-luminosity FR-II objects is dominated by radio lobes outside the central core. Similar to the radio-quiet Seyfert galaxies, one can distinguish in each case of the FR classes between Narrow-Line Radio Galaxies (NLRG) and Broad-Line Radio Galaxies (BLRG) which differ on their absorption level.
Blazars can be divided into two subclasses. BL Lac type objects exhibit only weak line emission, whereas the Flat Spectrum Radio Quasars (FSRQ) have strong broad emission lines in their optical spectra and show a compact radio structure. As will be described in the following section, blazars are characterised by the pointing of their relativistic jets into the observer's direction or at least close to it.

1.1.2. Unification Scheme

Figure 1.1 shows the most simplified model that tries to unify the different AGN types. It suggests a clear separation between the radio-loud and the radio-quiet sources according to the existence of beamed emission. Yet, it does not explain the origin and formation of a jet. About 10 percent of all known AGN are classified as radio-loud. They are furthermore divided into different ranges of luminosities which might be correlated with the mass and the spin of the central black hole. All other distinct appearances are traced to orientation effects. For instance, blazars are AGN with jets collimated towards the observer.
An AGN consists of several main components. The supermassive black hole is the central engine and is surrounded by plasma which collapses into an accretion disk orbitting the massive core. The central regions are obscured by an absorbing dust torus whose exact geometrical structure is believed to be rather clumpy than homogenous.
As pointed out in the previous section, some AGN spectra are characterised by broad, time variable emission lines in addition to less variable, forbidden lines with narrower Doppler widths. The distinct lines are expected to emanate from different regions. Reaching such large Doppler widths, the Broad-Line Region (BLR) is supposed to consist of hot, dense gas filaments or clouds located close to the central engine. In its gravitational field, the gas is accelerated to bulk motion. On the contrary, the gas of the Narrow-Line Region (NLR) must be in a different thermodynamic state. The emission of forbidden narrow lines indicates a lower density of the gas which is photoionized by the UV-X-ray continuum radiation emanating from the center. The NLR is probably much larger than the BLR since the variability time scales should scale with the size of the emitting area. The lack of broad lines in NLRGs can be explained by the orientation of the dust torus towards the observer. If the source is observed from the edge, the BLR is hidden by the absorber. However, its existence can be verfied by the fact that some Seyfert 2 galaxies show a broad-line component in polarized light which means that the BLR is indirectly visible through scattering in the NLR.
As mentioned before, the unification model basically only considers the absorbing material in the line of sight and the occurance of beamed emission. The intrinsic structure seems to be identical for all AGN. Yet, it might be reasonable to add further parameters like the black hole mass, the accretion rate and the luminosity in order to explain unresolved discrepancies and correlations like the decrease of variability with increasing luminosity. Apart from that, when aiming at the grand unification of black holes in the Universe, one has to clarify whether AGN are the bigger equivalents of Galactic Black Holes (GBHs). If so, AGN might as well exhibit cycles of activity accompanied by flux variations at various energies but on larger time scales than GBHs. We will have a closer look at the variability of blazars in the VHE regime after the following introduction to the observational techniques in the VHE astronomy.

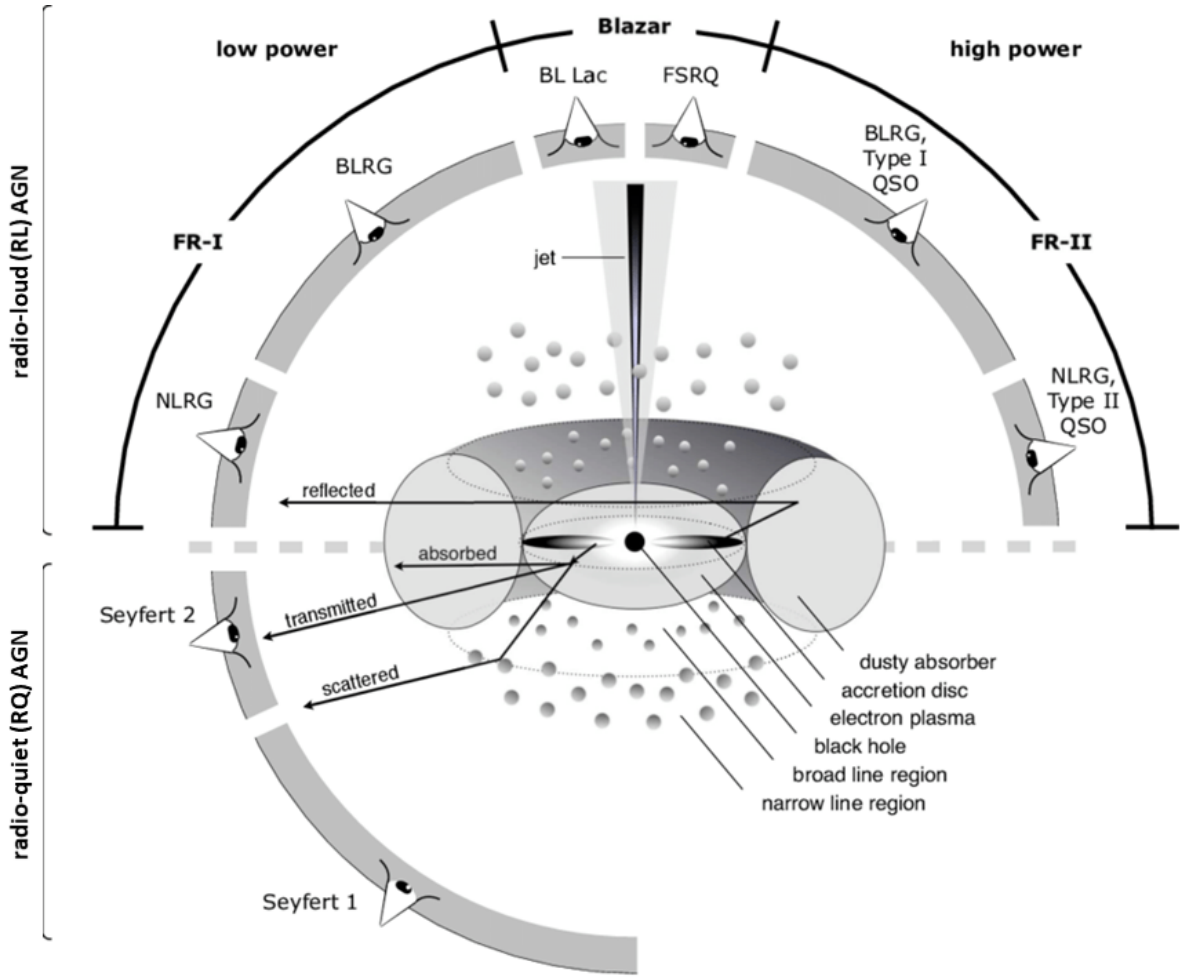

Figure 1.1.: Unification scheme showing the composition of an Active Galactic Nucleus (AGN). The classification of AGN is on one hand determined by the inclination angle between the rotation axis of the spinning central black hole and the observer. On the other hand, it is dependent on the formation of a jet (radio-loud AGN) and the general AGN power. The innermost region is surrounded by a dust torus which can absorb, transmit and reflect electromagnetic radiation emitted from the core where the central engine accumulates plasma on an accretion disk. Broad emission lines originate from the Broad-Line Region which consists of hot, dense gas. They are partly reflected in the Narrow-Line Region where gas of lower density causes narrow, forbidden emission lines. (Graphic by Marie-Luise Menzel taken from [5])

1.2. Very-High-Energy Astronomy

The higher the energy of photons emitted by astrophysical sources, the more difficult is their detection. Their number decreases with increasing frequency so that new instruments had to be designed for the observation of gamma rays. In the keV to GeV energy range, space-based telescopes like the Fermi Gamma-Ray Space Telescope are used since the atmosphere absorbs most of the electromagnetic radiation except visible light and radio waves (see Figure 1.2). The VHE regime covers energies above 100 GeV. Therefore, ground-based instruments which can detect VHE photons only indirectly are necessary since the detection surface of satellites is limited. Now that this challenging task has been mastered, the VHE astronomy offers great potential in revealing unexplained phenomena such as the variable emission of blazars. A successful indirect detection technique is to capture Cherenkov radiation which lays in the optical domain and is caused by atmospheric interaction of high-energy photons.

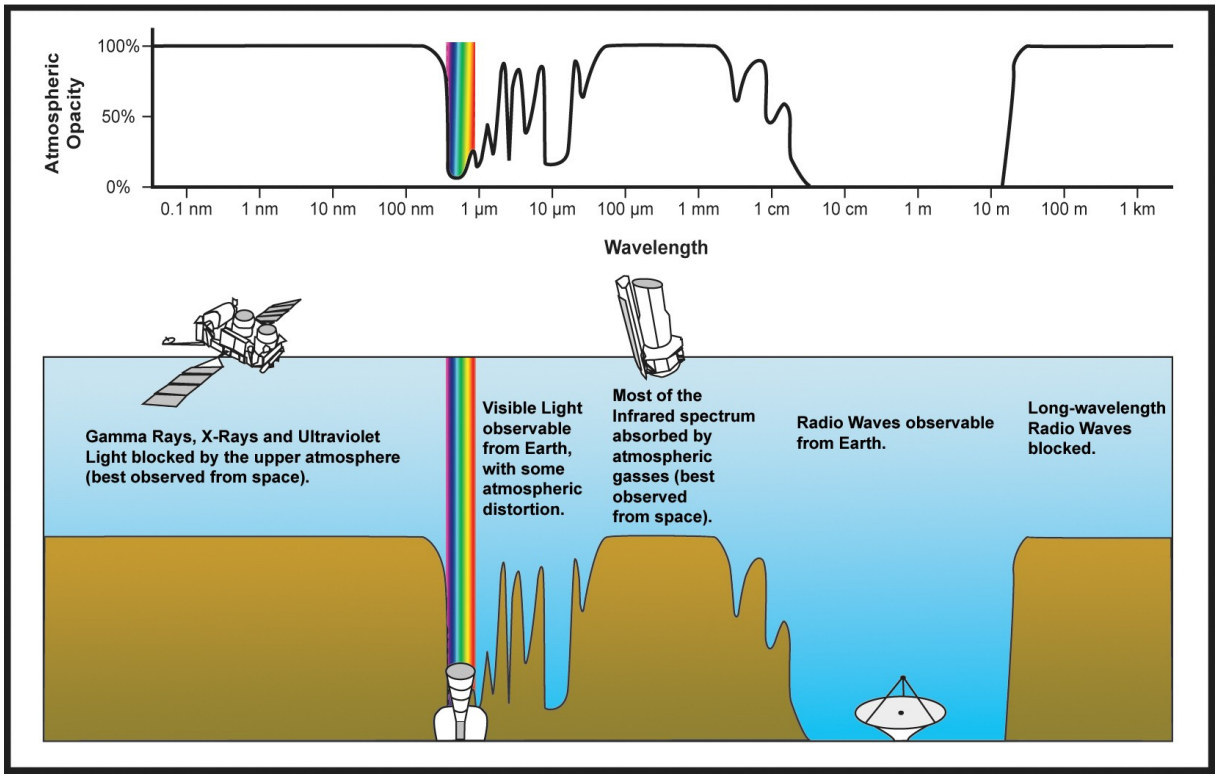

Figure 1.2.: Atmospheric opacity throughout the electromagnetic spectrum. Mainly visible light and radio waves can be observed by ground-based telescopes while other wavelengths have to be detected by space-based instruments or by indirect measurement methods. (Graphic taken from [7])

1.2.1. Imaging Atmospheric Cherenkov Telescopes (IACTs)

IACTs are designed to observe Cherenkov light flashes of air showers induced by gamma rays. Thereby, the atmosphere is a major component of the detector. When high-energy photons reach the Earth's atmosphere, they can produce electron-positron pairs while the conservation of momentum is given due to the interaction with massive particles such as atmospheric nuclei. Electrons and positrons interact with molecules as well, which leads to the emission of high-energy Bremsstrahlung. These secondary photons can trigger pair production again as long as their energy is above twice the electron's rest energy $2m_{\mathrm{e}}c^2$. As a consequence, an air shower propagates towards the ground until the energy losses due to pair production and Bremsstrahlung are equal. At a hight of about 10 km above sea level the density of particles reaches its maximum.
Cherenkov radiation is emitted by the atmospheric molecules if the velocity v of the charged particles of the shower exceeds the speed of light in the atmosphere which is a dielectric medium. Then, the molecules radiate because the induced polarization is asymmetric and therefore the waves do not cancel one another. Instead, the wavefronts form a light cone (see Figure 1.3) and the angle Θ between the trajectory of the charged particle and the direction of the emitted radiation can be calculated from:

$$\cos\Theta = \frac{1}{n\beta}, \tag{1.1}$$

where n is the refractive index of the atmosphere and $\beta = v/c$.
However, hadronic air showers triggered by cosmic-ray particles like protons or nuclei produce Cherenkov light as well while being more frequent than gamma-induced cascades. Aside from comprising electromagnetic showers, they are dominated by pion decays and appear broader and more scattered (see Figure 1.4).
The opening angle of the Cherenkov light cone in the atmosphere is about 1° which results in a light pool with a radius about 120 m at the height of about 2 km above sea level. The photon density depends on the energy of the primary gamma particle. To capture the faint Cherenkov light, a large reflection area is needed to focus the light onto the detection system (see Figure 1.5). IACTs require sensitive cameras and fast sampling electronics since the Cherenkov light flashes last only a few nanoseconds.
From the morphology of the measured light distribution, it is possible to distinguish hadronic from gamma-ray showers. The latter appear in elliptical shapes orientated towards the source, whereas events induced by cosmic particles are characterised by irregular images with several asymmetric islands (see Figure 1.6). As mentioned before, the IACT technique is an indirect observation of the gamma-ray sky. First, the gamma-ray events have to be filtered by means of the image shape. Then, the energy and direction of the primary photon of the air shower have to be reconstructed by means of Monte Carlo

simulations. Since IACTs operate in the optical domain, atmospheric conditions and ambient light limit the sensitivity and have to be taken into account. Apart from that, the Cherenkov light is attenuated increasingly for shower origins towards the horizon which requires also a correction for the zenith distance. Due to the numerous factors, it is extremely difficult to completely parametrise the atmosphere with its fluctuating conditions. For this reason, the calibration of the detector is often achieved by means of the signal from a stable, well known source which is used to determine the atmospheric conditions. In the X- and gamma-ray astronomy, the Crab Nebula usually serves as a calibration source and is used to convert the measured gamma rates into fluxes which are expressed in Crab Units (CU).

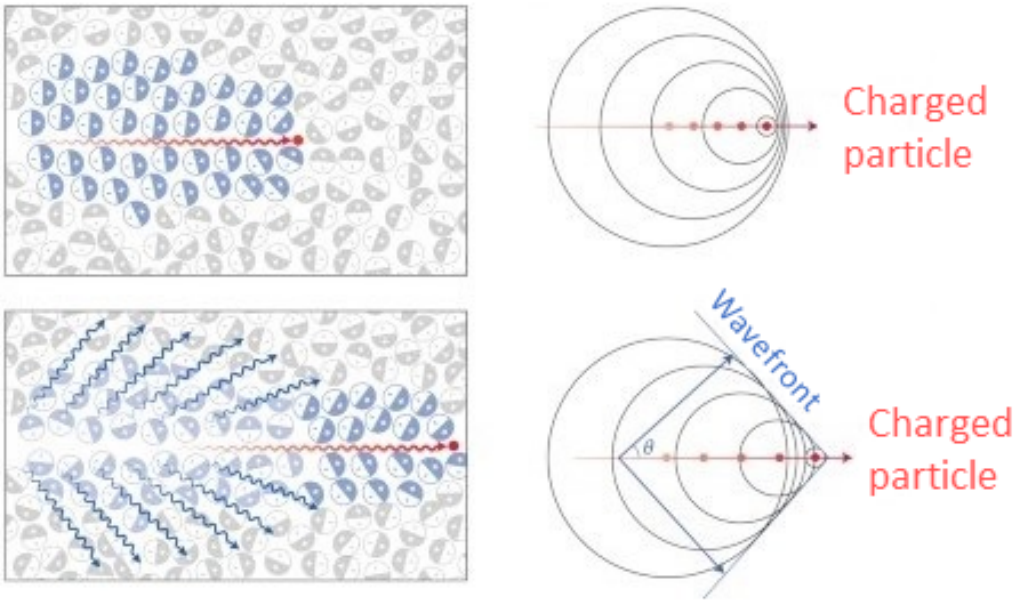

Figure 1.3.: Emergence of Cherenkov light. Molecules of a dielectric medium radiate if a charged particle faster than the speed of light in this medium passes. Then the induced polarization is asymmetric (see bottom left) and the resulting wave fronts form a light cone (see bottom right). At the top, the velocity of the charged particle is lower than the speed of light in the medium which results in a symmetric polarization. As a consequence, the waves cancel one another and no light is emitted. (Graphic taken from [8])

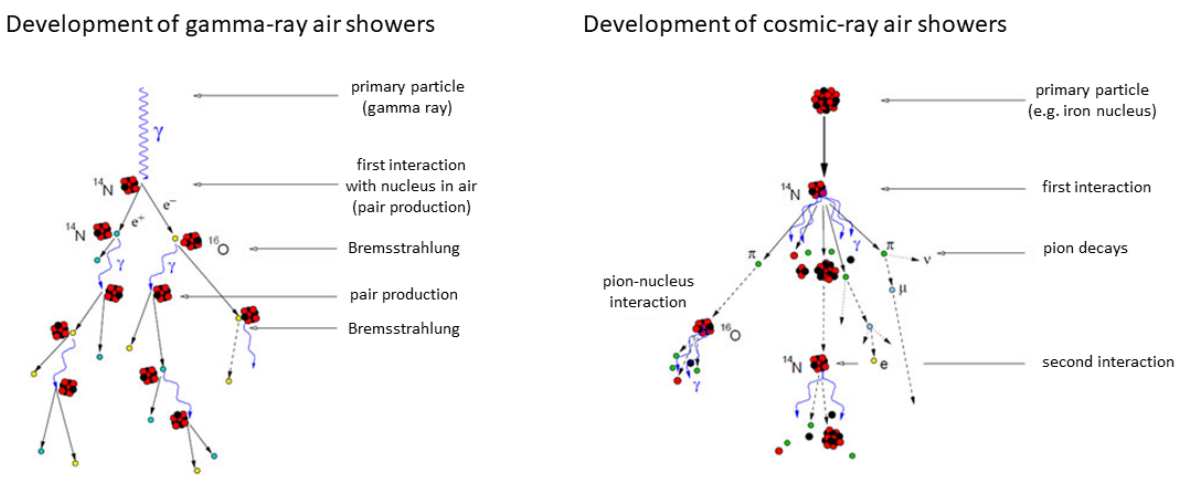

Figure 1.4.: Atmospheric particle showers. Left: Gamma-ray induced air showers propagate due to pair production and Bremsstrahlung. Right: Hadronic showers induced by cosmic-ray particles consist of electromagnetic showers and pion interactions and decays. Both types of particle cascades produce Cherenkov light. (Graphic by Konrad Bernlöhr, 1999, taken from `https://www.mpi-hd.mpg.de/hfm/CosmicRay/Showers.html`, 27.02.21)

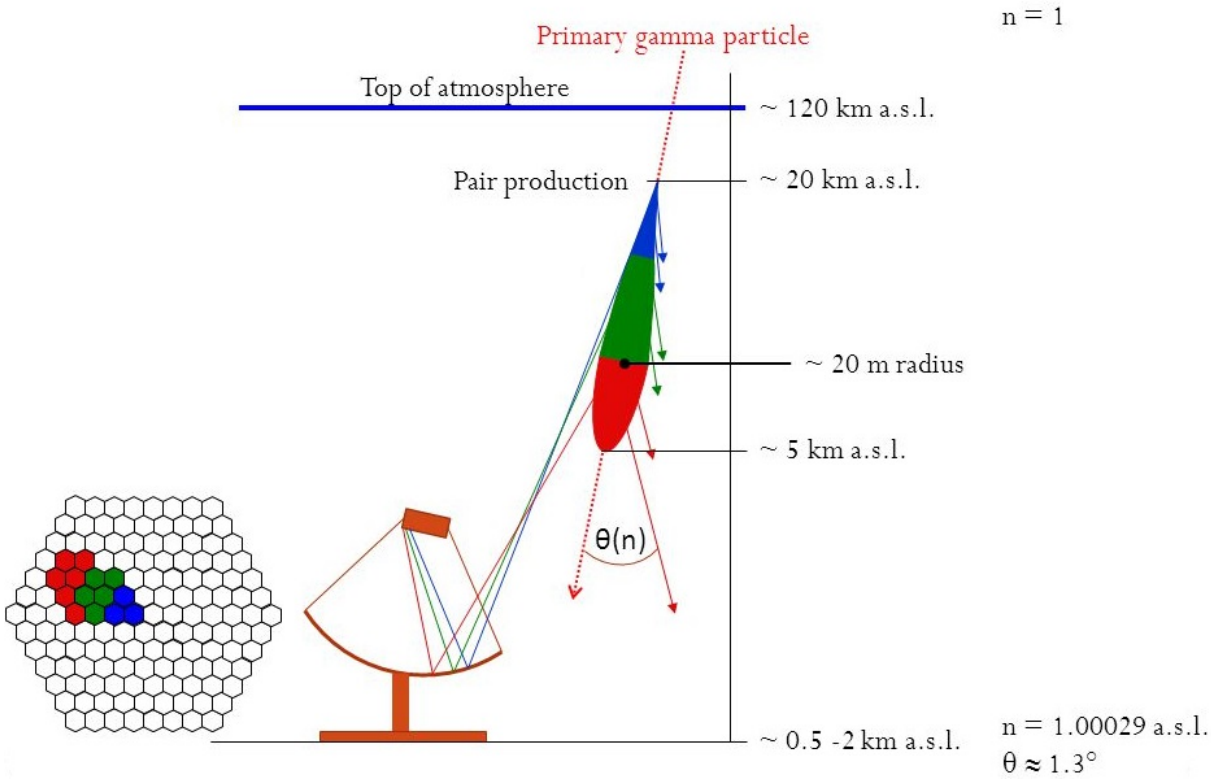

Figure 1.5.: Operating principle of an Imaging Atmospheric Cherenkov Telescope (IACT). The Cherenkov light produced in the higher atmosphere by air showers is reflected by a ground-based mirror and focussed onto the camera resulting in an elliptical shaped image. (Graphic by Arno Gadola, UZH, A new camera concept for Cherenkov telescopes, Zurich PhD seminar, August 2012)

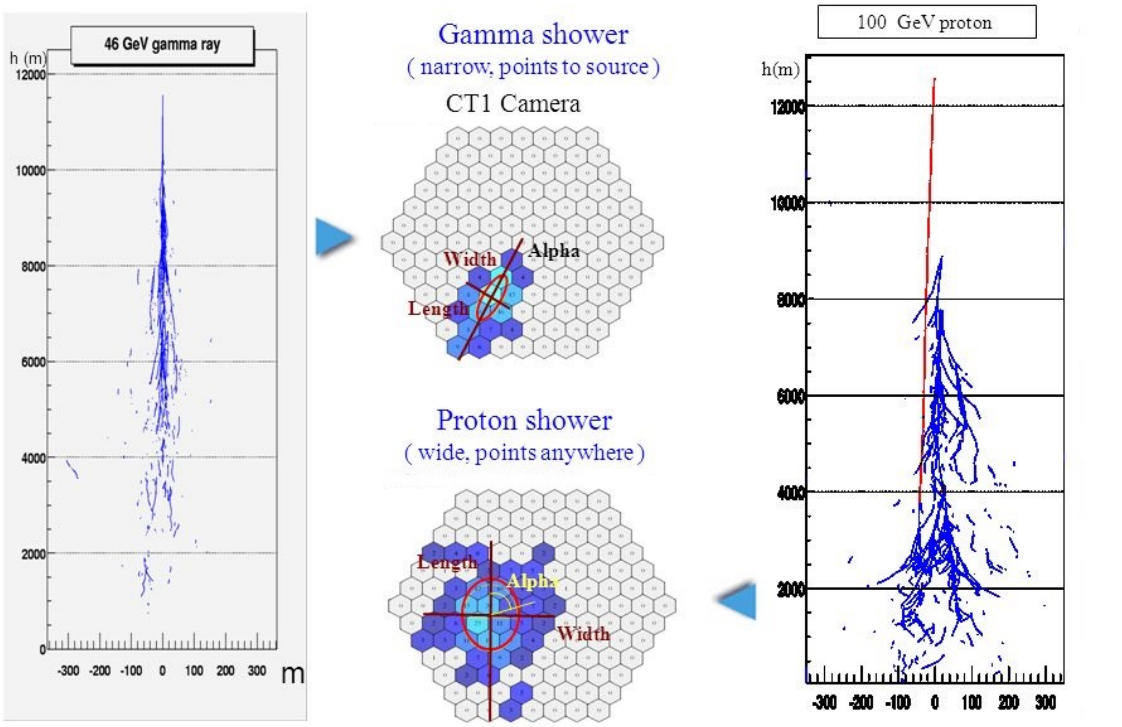

Figure 1.6.: IACT images originating from distinct air showers. Left: Gamma-ray showers result in elliptical shapes orientated towards the source. Right: Hadronic showers appear broader and more scattered and therefore show irregular images with asymmetric islands. (Graphic by Nadia Tonello, MPI for Physics, Munich, The islands method in the image analysis of atmospheric Cherenkov Telescopes data, DPG Spring Meeting 2004)

1.3. Blazar Emission Models

1.3.1. Production of Gamma Radiation

In the VHE regime, the extragalactic sky is dominated by blazars, in particular by the high-energy peaked BL Lac type objects. The Spectral Energy Distribution (SED) of blazars is governed by the beamed, non-thermal emission and characterised by a two-hump structure reflecting the synchrotron and inverse Compton branch (see Figure 1.7). Other emission components like thermal radiation from the accretion disk or emission lines can barely be detected although assumed to be present. The first hump is caused by charged particles accelerated in a magnetic field, thus emitting polarised synchrotron radiation in the optical to X-ray range. The second hump peaking at higher frequencies in the gamma-ray regime is commonly traced back to the scattering of photons to higher energies by relativistic particles through the inverse Compton process.

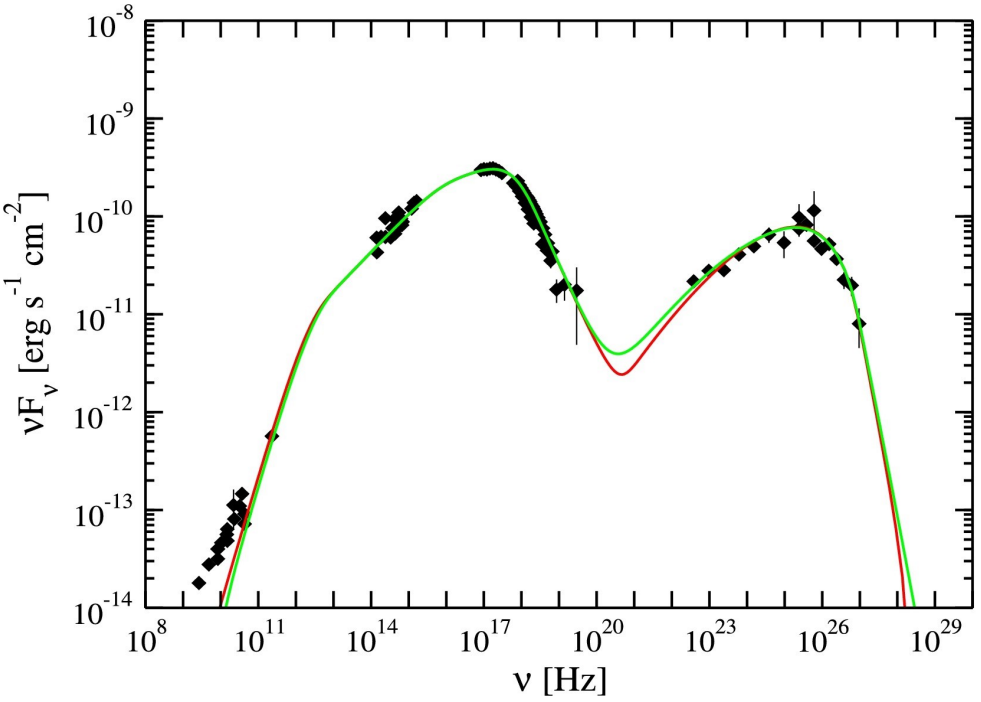

Figure 1.7.: Spectral Energy Distribution (SED) of Mrk 421 as measured during a multiwavelength campaign including Fermi and MAGIC gamma-ray telescopes. The green and red lines are two different SSC model fits. The characteristic two-hump structure reflecting the synchrotron and inverse Compton branch is visible. (Graphic taken from [9])

BL Lac type objects peak in the X-ray and VHE range respectively, but show lower luminosities than FSRQ which in turn have lower peak frequencies. So far, it is not clear which physical parameters determine these peak frequencies, but it is assumed that the jet power plays an important role. A weaker jet might be correlated with a lower particle density leading to a high-peaked spectrum as it is the case for BL Lac Blazars. The

cooling process of a smaller amount of electrons is less efficient. As a consequence, more particles reach high energies and can produce high-frequency synchrotron radiation.
According to the synchrotron self-Compton (SSC) model, the VHE peak results from the up-scattering of the synchrotron photons in the jet via the inverse Compton process. On the contrary, the external Compton (EC) model suggests that also photons from the surrounding area can be up-scattered which would leave more free parameters. Figure 1.8 shows schematically inverse Compton processes in the jet of a blazar, considering both the SSC and EC model, leading to the emission of high-energy radiation. Observations of correlated gamma- and X-ray emission support this approach [10].

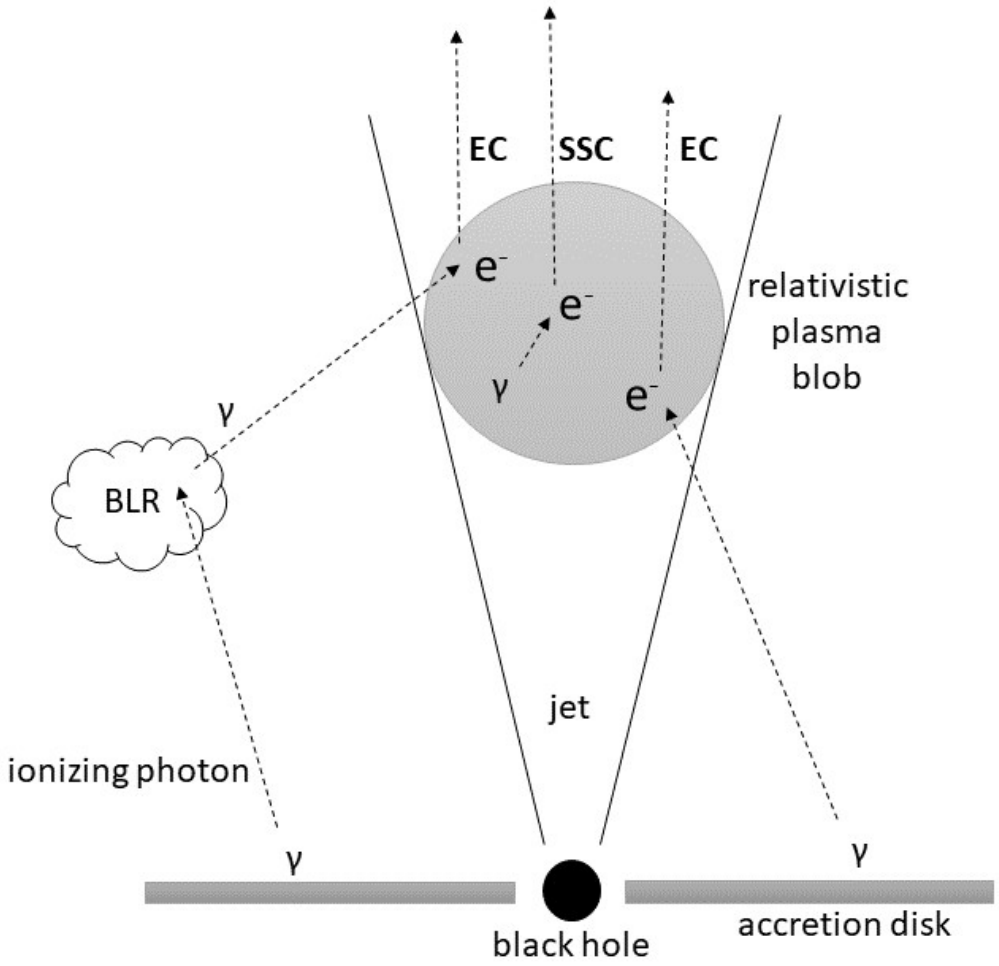

Figure 1.8.: Inverse Compton scattering in the jet of a blazar. Relativistic electrons inside plasma blobs are ejected along the beamed emission and produce synchrotron photons through interaction with magnetic fields. Besides synchrotron self-Compton (SSC) processes inside the jet, the external Compton (EC) model suggests that external seed photons, for example from the Broad-Line Region (BLR) or the accretion disk, can gain energy through scattering by the relativistic electrons. (Graphic taken from [5])

However, it is not clear whether the relativistic electrons are responsible for the high-energy emission. Instead of leptonic origin, hadronic models are possible. Accordingly, high-energy photons could emerge from proton synchrotron radiation or secondary emission from photo-pion and pair production processes. The detection of neutrino emission would support hadronic models.
Probably, AGN jets consist of both leptons and hadrons and several processes contribute to some extent to the characteristic gamma-ray emission of blazars. Beside the composition of the jet and the underlying physical processes, the spatial origin and the question of whether there are multiple emission regions still have to be investigated. Especially, the extreme variability of the gamma-ray emission so far defies a compelling physical interpretation. Shock waves propagating along the relativistic jet are likely to be a crucial factor and they could explain distinct flux states by relativistic beaming effects.

1.3.2. Relativistic Beaming

Relativistic beaming occurs in many astrophysical phenomena, among them in relativistic jets of AGN. The basic principle is explained below, following the description by Choudhuri's textbook [11]. We consider an object moving with velocity v while emitting a beam of light in an angle $\Theta^{'}$ with respect to its direction of motion. From the observer's frame, the beam appears at the angle Θ which is in general smaller than $\Theta^{'}$:

$$\tan\Theta = \frac{\sin\Theta^{'}}{\gamma(\cos\Theta^{'} + \beta)}\,, \tag{1.2}$$

where $\beta = v/c$ and γ is the Lorentz factor $1/\sqrt{1-\beta^2}$. From the special case of $\Theta^{'} = \pi/2$ corresponding to an emission perpendicular to the object's direction of motion:

$$\tan\Theta = \frac{c}{\gamma v}\,, \tag{1.3}$$

one can derive that for highly relativistic objects ($v \sim c$ and $\gamma \gg 1$) Θ is a small angle of the order $1/\gamma$. This means that even if the radiation is emitted in different directions by the object, it appears to the observer that all light is emitted in the forward direction of the object's motion within a cone of angle $1/\gamma$. Relativistic beaming is also known as Doppler boosting because the observed luminosity is determined by the relativistic Doppler effect.

1.3.3. Variability and Flux States

The variability time scales generally mirror the dynamical time scales of the system and therefore rapid variations in the observed radiation indicate compact emission sites. Blazars show particularly at TeV energies high variability down to minute time scales.
Blandford and Königl [1] predicted that particles are accelerated at shock waves appearing as enhanced emission in small regions (knots) within the jet. These knots often exhibit apparent superluminal motion from the observer's point of view. It is still uncertain how shocks are formed in relativistic plasma outflows except that the relative fluid velocity must exceed the local sound speed and that the knots are likely to arise from the active center of the AGN.
Figure 1.9 shows a shock travelling down the collimated outflow. The electrons with the highest energies emitting synchrotron radiation in the gamma-ray regime are directly behind the shock front. Relativistic beaming affects the observed emission and could explain distinct flux states. Blazars in active states show a flaring behaviour characterised by high-amplitude fluxes resulting from the Doppler boosting of the emission from the fastest shocks. On the contrary, the nonflaring state is governed by low fluxes. Thereby, multiple shocks from the decelerated jet further downstream produce an apparently steady baseline emission with weaker Doppler boosting.
Studying the shape of flux distributions provides crucial information for testing this scenario.

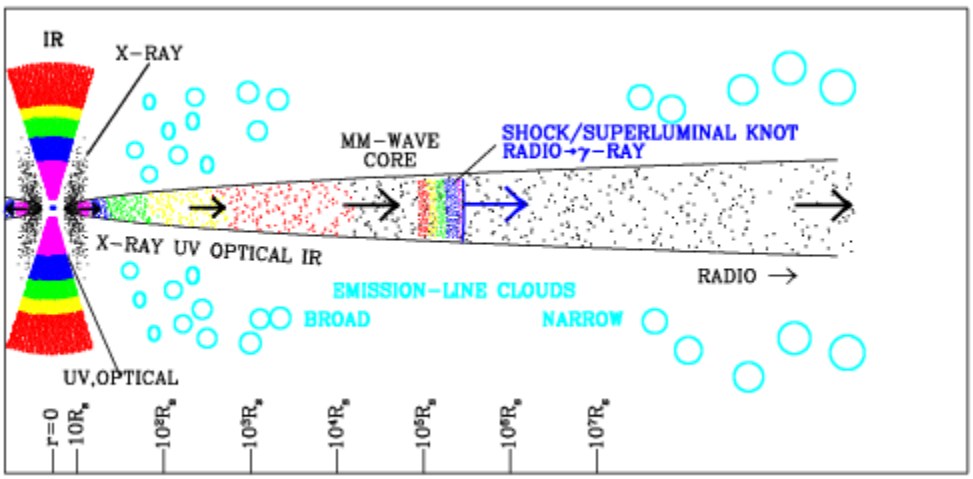

Figure 1.9.: Propagation of a shock wave along the jet of an AGN. The density of the dots reflects the intensity of the emission and the different colours represent the corresponding emission frequencies. The energy of the thermal radiation from the accretion disk is the higher, the closer to the black hole. The jet is mostly characterised by radio emission except at superluminal knots where the energy density is stratified. High-energy particles directly behind the shock front radiate gamma-rays. (Graphic by Alan Marscher, Boston University Blazar Group, taken from `https://www.bu.edu/blazars/research.html`, 27.02.21)

2. Investigation of Flux Distributions

2.1. Interpretation of Flux Distributions

Since it is not possible to observe the underlying physical processes in astronomical sources directly, statistical properties of observable quantities can provide further insights into the system. Flux variations are used to derive physical mechanisms causing variable emission. Yet, one can not draw unambiguous conclusions from mere statistical properties since the number of mathematical models based on light curve analysis reproducing the observed fluxes can be large. In his enquiry concerning, among other things, log-normal flux distributions, J.D. Scargle pointed out that "elucidating complex, dynamic, three-dimensional astrophysical systems - with uncertain physical processes and parameters - from one-dimensional time series data is intrinsically difficult" [2].
However, it is crucially important to intensively study the statistics of the measured light curves on different time scales. Especially in the VHE regime, the available data and previous results are limited and need further investigations. Revealing the existence of distinct flux states will be a major step forward in solving the complex combination of physical processes. In the following, possible components of flux distributions and their interpretation are described.

2.1.1. Normal Distribution

The probably most common type of distribution is the normal or Gaussian distribution which is characterised by its symmetric bell shape with a certain mean value and width. For example, pure random variations of a measurand follow a normal distribution. Apart from that, the Gaussian plays a key role in the superposition of effects. According to the central limit theorem the summation of a large number of independent systems converges towards a normal distribution regardless of the distributions of the individual components. This is why Gaussian distributions are often associated with additive processes. In the case of AGN, the normally distributed fluxes could result from the superposition of many different emission zones or processes although the question arises whether modeling the observed flux as an outcome of separated independent origins is a realistic approach.
If the flux distribution shows a Gaussian component, it corresponds most suitably to a steady baseline flux and thus can be identified with the ground state of the blazar. One

also has to keep in mind the detector systematics that are also likely to be expressed by a Gaussian (see Section 2.2.2). Consequently, one can define only an upper limit for the baseline flux of the ground state due to the limited sensitivity [4, 3]. However, the majority of flux distributions deviate from a Gauss curve because of a tail with high fluxes which occur from individual flare events.

2.1.2. Log-Normal Distribution

A log-normal distribution is positively skewed which means that the right tail towards higher fluxes is longer which makes the log-normalcy suitable for the inclusion of high-amplitude flares. Analogous to the sum of independent events resulting in a Gaussian, a log-normal distribution can be generated by multiplying the effects of many independent subsystems. This follows directly from the central limit theorem because the logarithm of a log-normally distributed variable follows a normal distribution. Many natural phenomena are driven by multiplicative stochastic processes and thus show a log-normal behaviour. Log-normal flux distributions of blazars might indicate cascade-like emission but do definitely not rule out additive models which can produce as well log-normal-like distributions as J.D. Scargle proved in his aforementioned enquiry [2]. He stated that "log-normalcy is not magical", which means that it is not ultimately contingent on a physical mechanism.
So far, log-normal variability has been discovered in X-ray light curves and is commonly associated with accretion disk fluctuations [12, 13]. Possible scenarios are log-normal variations in the viscosity parameter or in the accretion rate which propagate through the disk and affect the plasma injection rate of the jet [14]. Variability on different time scales reflects fluctuations at different radii [15]. Faster variations in the accretion rate are expected to occur at radii closer to the central engine. However, the interpretation of the extremely short variability time scales in the VHE regime remains difficult when sticking to this scenario.
The variations on minute time scales of blazars are very likely related to relativistic beaming effects due to the direct pointing of the jet towards the observer. The fastest shocks propagating along the jet emit highly Doppler boosted radiation. The resulting high-amplitude fluxes are well incorporated in the distribution by a log-normal component which is thus an imprint of the flaring state of the blazar.
Within this analysis, the question of whether the flux distributions of the blazars Mrk 421 and Mrk 501 can be described by a normal and/or log-normal component will be addressed. This project requires data which is acquired in an unbiased way. Whereas large IACTs often trigger observations on high fluxes, the first G-APD Cherenkov Telescope (FACT) (see Figure 2.1) provides long-term data without any bias towards higher fluxes.

Figure 2.1.: The first G-APD Cherenkov Telescope (FACT) on La Palma. It has a small mirror area of 9.5m^2 and uses silicon-based photosensors what makes FACT optimal for long-term and continuous monitoring of a small sample of gamma-ray sources. (Photo by Miguel Claro, Art Science Photography, 2013, taken from `https://www.miguelclaro.com/wp/portfolio/fact-cherenkov-telescope-dragged-milky-way/`, 27.02.21)

2.2. Properties of FACT Data

FACT is a relatively small IACT located at La Palma with a mirror area of $9.5\,\mathrm{m}^2$. The energy range of the instrument covers the VHE domain above 0.3 TeV. Instead of conventional photo multipliers, its camera uses Geiger-mode Avalanche Photo Diodes (G-APDs) which significantly improve sensitivity. The new technology of silicon-based photosensors enables observation despite bright light conditions like moonlit nights and thus makes FACT optimal for continuous monitoring. This is crucial for studying the temporal evolution of highly variable gamma-ray sources such as blazars. Since October 2011, FACT is monitoring in an unbiased manner a small sample of sources [16].

2.2.1. Observational Effects

FACT data can be expressed in excess rates whereby an excess is defined as the difference between signal and background. The signal is calculated according to the orientation of the resulting IACT image (see Figure 1.6) [17]. Depending on the time binning, the rate is determined through dividing by a certain observation time (e.g. 1 night). Ambient light and atmospheric conditions influence substantially the detection of faint Cherenkov light flashes. Due to its constant flux density and spectrum in the VHE regime, the Crab Nebula serves as a calibration source to correct the light curves for the effects of zenith distance (zd) and trigger threshold (th) and to convert the measured excess rates into fluxes. A brighter night-sky background, mainly ruled by the moon cycle, results in a higher trigger threshold and thus in a reduced gamma-ray rate. The threshold can be determined through ratescans. Therefore, the detector's trigger rate is measured as a function of the trigger threshold. At low thresholds the rate is dominated by ambient photons of the night-sky background, whereas at high thresholds photons from particle showers induced by cosmic rays dominate. The intersection point of the falling edge of night-sky background and the tail representing the constant cosmic-ray rate is used as trigger threshold. Knowing the correlation between amount of ambient light and the current measured in the camera, the trigger threshold can be calibrated and set according to the measured currents [18]. In addition, there is an increasing attenuation of Cherenkov light for shower origins towards the horizon. As a consequence, the rate decreases with larger zenith distances [19].
The fluxes have been corrected for such observational effects. In order to check the applied data correction algorithm for the effects of zenith distance and trigger threshold, the distribution of nightly binned fluxes of the Crab Nebula is examined (see Figure 2.2). One expects the fluxes of this stable source to be normally distributed with a mean value of one Crab Unit (CU). However, there are deviations towards the edges of the distribution and the mean value of the fitted Gauss curve is smaller than one CU (see Figure 2.2 a). Obviously, the correction of the data is not optimal yet. If now only fluxes with small zenith

distances (zd $< 30°$) and low trigger thresholds (th < 350 dac counts) corresponding to good observation conditions are selected, we obtain a well Gaussian-shaped distribution, but its mean value is still too small (see Figure 2.2 b). This leads to the conclusion that the fluxes are slightly overcorrected towards lower fluxes.

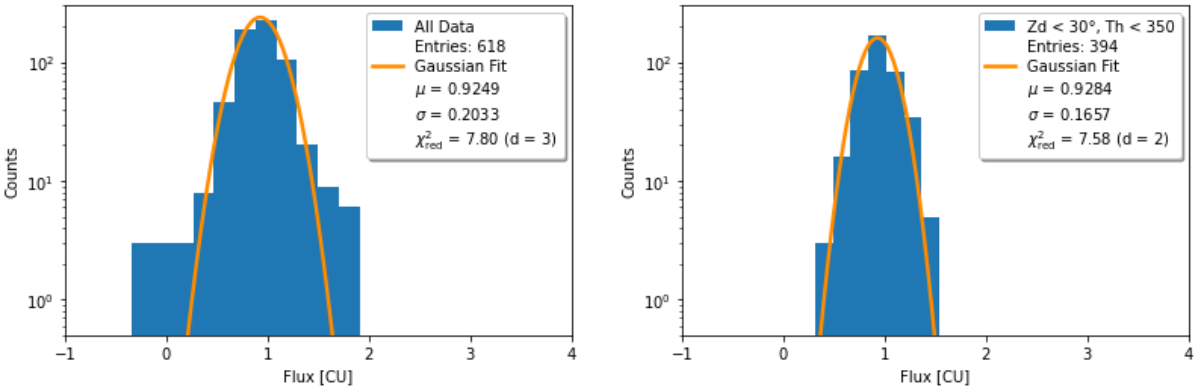

(a) Especially for negative fluxes the distribution differs from the expected normal distribution with $\mu = 1\,\mathrm{CU}$.

(b) The data is well normally distributed after selecting only fluxes with zenith distances under 30° and trigger thresholds under 350 dac counts. The mean value μ is still too small.

Figure 2.2.: Distribution of nightly fluxes of the Crab Nebula as measured by FACT from 2011 to 2019. The Gaussian fit with mean value μ and standard deviation σ is indicated by the orange line.

2.2.2. Detector Systematics

The flux distribution of every measurement is folded with the distribution of the background and detector systematics. To be able to quantify these fluctuations, one can use the width of the flux distribution of the narrow-line Seyfert 1 galaxy 1H0323+342 which could not be detected by FACT according to the low significance ($1.06\,\sigma$)[1] of its signal. As expected the mean value of the fitted normal distribution is almost zero and the standard deviation $\sigma = 0.14\,\mathrm{CU}$ reflects rather the measurement uncertainty due to the detector systematics than properties of the source itself (see Figure 2.3 a). Yet, there could be a hint of signal from the source in the form of a small bump towards higher fluxes which even remains after applying the same data selection cut as for the Crab Nebula (see Figure 2.3 b).

[1]FACT Database Explorer, 1H0323+342: `https://www.fact-project.org/dch/db_explorer.php?short=11383`, 14.02.2021

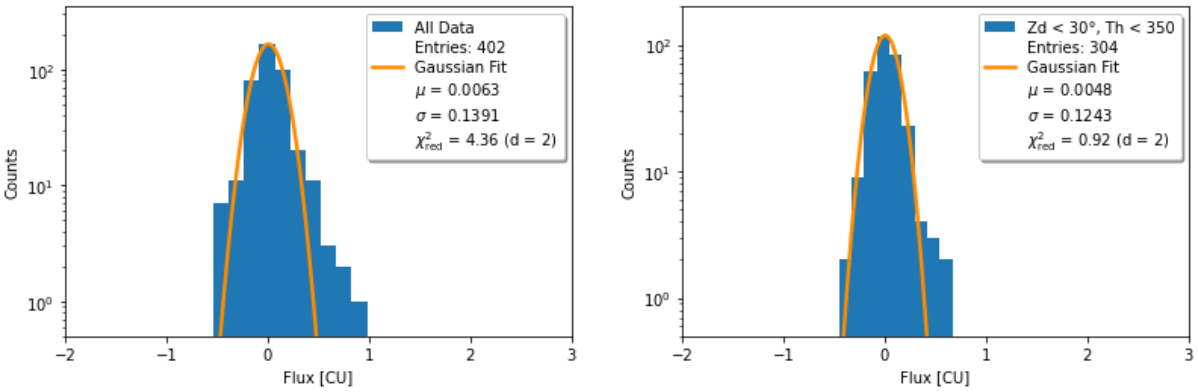

(a) The width of the distribution mainly results from background fluctuations and detector systematics although deviations from the Gaussian distribution especially towards higher fluxes are visible.

(b) There is still a hint of signal after selecting only fluxes with zenith distances under 30° and trigger thresholds under 350 dac counts.

Figure 2.3.: Distribution of nightly fluxes of the non-detected source 1H0323+342 as measured by FACT from 2013 to 2019. The Gaussian fit with mean value μ and standard deviation σ is indicated by the orange line.

2.2.3. Sample and Data Selection

In order to explore the variability of blazars in a systematic way, high statistics measurements as FACT provides for a small sample of sources are necessary. Among the monitored objects are Mrk 421 and Mrk 501, the brightest known astrophysical sources at TeV energies. They are classified as high-frequency peaked BL Lac blazars and show highly variable emission in the radio to VHE range. Due to their brightness and relative proximity, they have been detected by all ground-based gamma-ray instruments. It is a meaningful strategy to study well-known objects such as Mrk 421 and Mrk 501 in order to be able to derive physical properties and in a next step to check whether the gained knowledge applies to other blazars as well.

In this analysis, the distributions of fluxes of Mrk 421 and Mrk 501 as measured by FACT from 2012 to 2019 are examined with regard to the underlying shape. The used FACT data have been analysed as described in [17] and corrected for observational effects like zenith distance and trigger threshold. After applying a data quality check based on the cosmic-ray rate as described in [20, 21], the data sample comprises 786 nights (1882 hours in total) for Mrk 421 and 896 nights (1725 hours in total) for Mrk 501. Figure 2.4 shows the light curves of the nightly binned fluxes of both sources. It can be seen that Mrk 421 shows during the whole observation period a variable emission whereas the flux level of Mrk 501 decreased significantly over the years. The observation period of Mrk 501 can be divided into an active phase from 2012 to 2016 and into a low phase from 2017 to 2019 when the source was almost below the detection threshold. Mrk 501 will be further investigated regarding its temporal evolution within the analysis of the flux distributions

for the individual years.

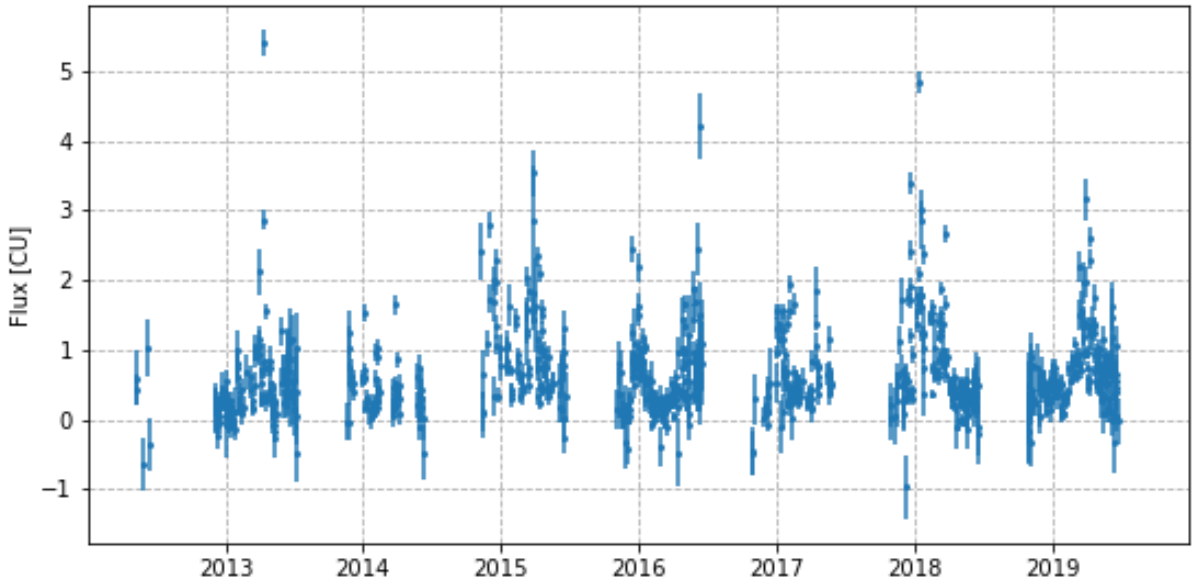

(a) Mrk 421

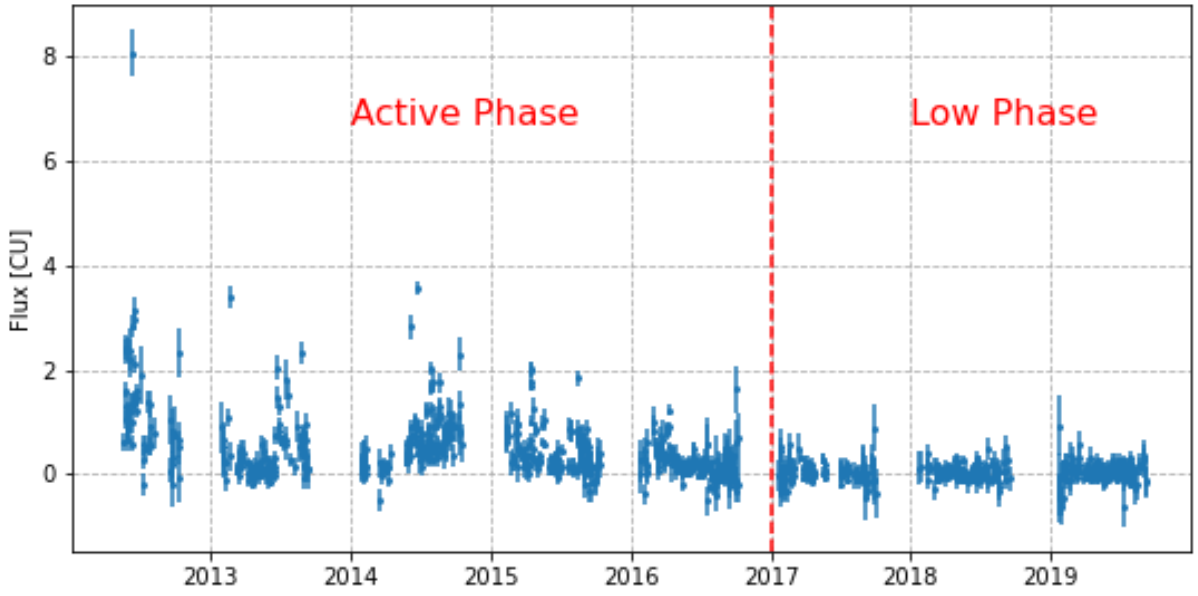

(b) Mrk 501

Figure 2.4.: Light curves of nightly binned fluxes as measured by FACT from 2012 to 2019

2.3. Method

Searching for suitable distribution functions to describe the observed fluxes is one aim of this work, but probing the effects of different binnings is equally important. This refers both to the time binning of the light curves and to the binning of the histogram. In this way, statistical properties are compared on different time scales and tested for their significance.

2.3.1. Statistical Considerations

For the regular binning, the bin width corresponds to the averaged error of the data set so that mere statistical fluctuations do not affect the distribution. The distribution functions described in Section 2.3.3 are fitted to the points at the top centers of the histogram bins[2]. When fitting discrete distributions such as of the observed fluxes, one theoretically would have to find the optimal fit function by minimizing the difference between bin area and the area under the curve in the range of the bin instead of the difference between points. However, the areas align quite well when the fitted curve crosses the center of the bin.
In order to evaluate the goodness of fit, a chi-squared (χ^2) test is performed. For each category i, the difference between the observed frequency $f_\mathrm{i}^\mathrm{obs}$ and the expected frequency $f_\mathrm{i}^\mathrm{fit}$ is calculated. The deviation of the observed from the fitted distribution is evaluated by the quantity:

$$\chi^2 = \sum_\mathrm{i} \frac{(f_\mathrm{i}^\mathrm{fit} - f_\mathrm{i}^\mathrm{obs})^2}{f_\mathrm{i}^\mathrm{fit}} \,. \tag{2.1}$$

The expected frequency $f_\mathrm{i}^\mathrm{fit}$ can be calculated by multiplying the area under the probability density function (PDF) in the range of the category i with the total number of histogram entries N:

$$f_\mathrm{i}^\mathrm{fit} = N \int \mathrm{pdf}\, dx = \int \frac{\mathrm{fit}}{\Delta x}\, dx \,, \tag{2.2}$$

whereby the fit function has to be scaled with the bin width Δx and the total number of entries N in oder to get a dimensionless PDF. To be able to assume a chi-squared distribution for the test quantity χ^2, the typical rule is that all frequencies should be at least five, which in most cases could be achieved by combining several bins at the edges of the fitted distribution to one category. The Python implementation of the χ^2 test for any continuous distribution function is included in Appendix A.2. In order to be able to

[2]Utilized implementation: `https://docs.scipy.org/doc/scipy/reference/generated/scipy.optimize.curve_fit.html`, 14.02.2021

compare different fit functions the reduced χ^2_{red} is calculated:

$$\chi^2_{\text{red}} = \frac{\chi^2}{d}\,, \tag{2.3}$$

where d is the number of degrees of freedom which is the number of categories minus the number of fit parameters.

2.3.2. Bayesian Binning

In contrast to the regular binning, Bayesian bins are "neither constrained to be equal nor is their number or size pre-defined" [22]. The Bayesian Block algorithm that Scargle et al. developed in 2013 finds the optimal binning by fitting the best step function to the ordered data [22]. The advantage of this method is that the data are represented with their significant features as well as possible without losing information due to arbitrarily chosen bins. Figure 2.5 demonstrates the principle of Bayesian binning by means of example data.

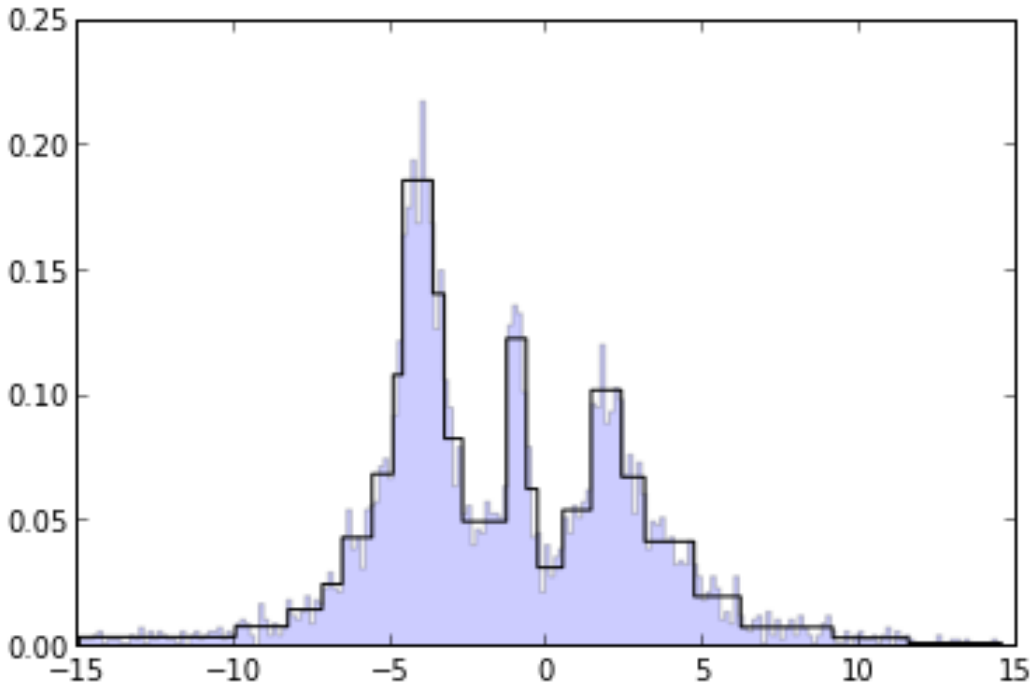

Figure 2.5.: Bayesian binning demonstrated by means of example data. Although the bin width of the colored histogram is much smaller, the Bayesian bins in black still represent all important features of the data. (Graphic by Jake VanderPlas, Pythonic Perambulations, 2012, taken from `https://jakevdp.github.io/blog/2012/09/12/dynamic-programming-in-python/`, 27.02.21)

The Astropy histogram function[3] provides the option of using bins that are calculated by the Bayesian Block algorithm[4]. The false positive rate p_0 is the probability of falsely reporting the detection of a change point between two bins. It is used as a parameter to define the fitness algorithm which is left in its default settings (event data and $p_0 = 1\%$) for this analysis.

2.3.3. Fit Functions

The following distribution functions are tested for describing the observed fluxes. The Gaussian component is modelled by the fit function:

$$f_{\text{gauss}}(x) = a \exp\Big[-\frac{(x-\mu)^2}{2\sigma^2}\Big], \tag{2.4}$$

where μ, σ and a are the mean value, the standard deviation and the stretching parameter. Whereas the normal distribution is symmetrical around the mean value μ, the log-normal distribution is asymmetrical and only defined for positive variables. As the background has to be subtracted from the measured signal, fluctuations can lead to negative fluxes. In order to be able to fit a log-normal distribution to the data, one has to add an offset s to the fit function:

$$f_{\log}(x) = \frac{a}{\sigma(x-s)} \exp\Big[-\frac{(\ln(x-s)-\mu)^2}{2\sigma^2}\Big], \tag{2.5}$$

with a, μ and σ being the stretching parameter and the mean value and standard deviation of the normally distributed logarithm. When the shift s is implemented as an additional parameter of the fit function, the program was not able to optimise the fit parameters. Therefore, the offset s was set to the minimum flux value of the data to avoid negative arguments of the logarithm. The combination of the normal and log-normal components thus leaves six parameters to modify the fit function:

$$f_{\text{combi}}(x) = f_{\text{gauss}}(x) + f_{\log}(x)\,. \tag{2.6}$$

[3] `https://docs.astropy.org/en/stable/api/astropy.visualization.hist.html`, 14.02.2021
[4] `https://docs.astropy.org/en/stable/api/astropy.stats.bayesian_blocks.html`, 14.02.2021

Another way to obtain positive skewness is the Exponentially Modified Gaussian (EMG) distribution[5] consisting of an exponential and a complementary error function[6]:

$$f_{\mathrm{EMG}}(x) = a \exp\Big[\frac{\lambda}{2}(2\mu + \lambda\sigma^2 - 2x)\Big] \operatorname{erfc}\Big[\frac{\mu + \lambda\sigma^2 - x}{\sqrt{2}\sigma}\Big], \tag{2.7}$$

with the four parameters a, μ, σ and λ being used to stretch, shift, scale and shape the fit function. The EMG distribution describes the sum of independent normal and exponential components and thus can be obtained by the convolution of their distributions. In the above parameterization, μ and σ correspond to the mean value and standard deviation of the Gaussian variable and λ to the rate of the exponential component.
The approach in the next sections is to fit the four above distribution functions to the respective data set and then to find out which one shows the smallest χ^2_{red} and thus describes the data best for the present histogram and time binning properties. An overview of all parameters for each plot is included in Appendix A.1.

2.4. Results Mrk 421

In the following, the different binning effects are discussed in detail by means of the flux distributions of Mrk 421.

2.4.1. Regular Binning

The distribution of the nightly binned fluxes of Mrk 421 with equal bins as wide as the mean error differs at first glance from a Gaussian, which is also expressed by the large $\chi^2_{\mathrm{red}} = 123.26$ of the normal fit (see Figure 2.6a). The log-normal fit with $\chi^2_{\mathrm{red}} = 59.82$ (see Figure 2.6b) is obviously not skewed enough to reasonably describe the data. A significant improvement of $\chi^2_{\mathrm{red}} = 2.33$ is achieved when fitting the combination of the normal and log-normal distributions (see Figure 2.6c). From the peak and the tail with higher fluxes, one can see immediately that the distribution function, which consists of two components and thus six fit parameters, is more suitable. Almost as good is the EMG fit with $\chi^2_{\mathrm{red}} = 2.52$ (see Figure 2.6d) which also shows a distinct positive skewness.

[5] `https://docs.scipy.org/doc/scipy/reference/generated/scipy.stats.exponnorm.html`, 14.02.2021

[6] $\operatorname{erfc}(x) = 1 - \operatorname{erf}(x) = \frac{2}{\sqrt{\pi}} \int_x^\infty \mathrm{e}^{-t^2} dt$

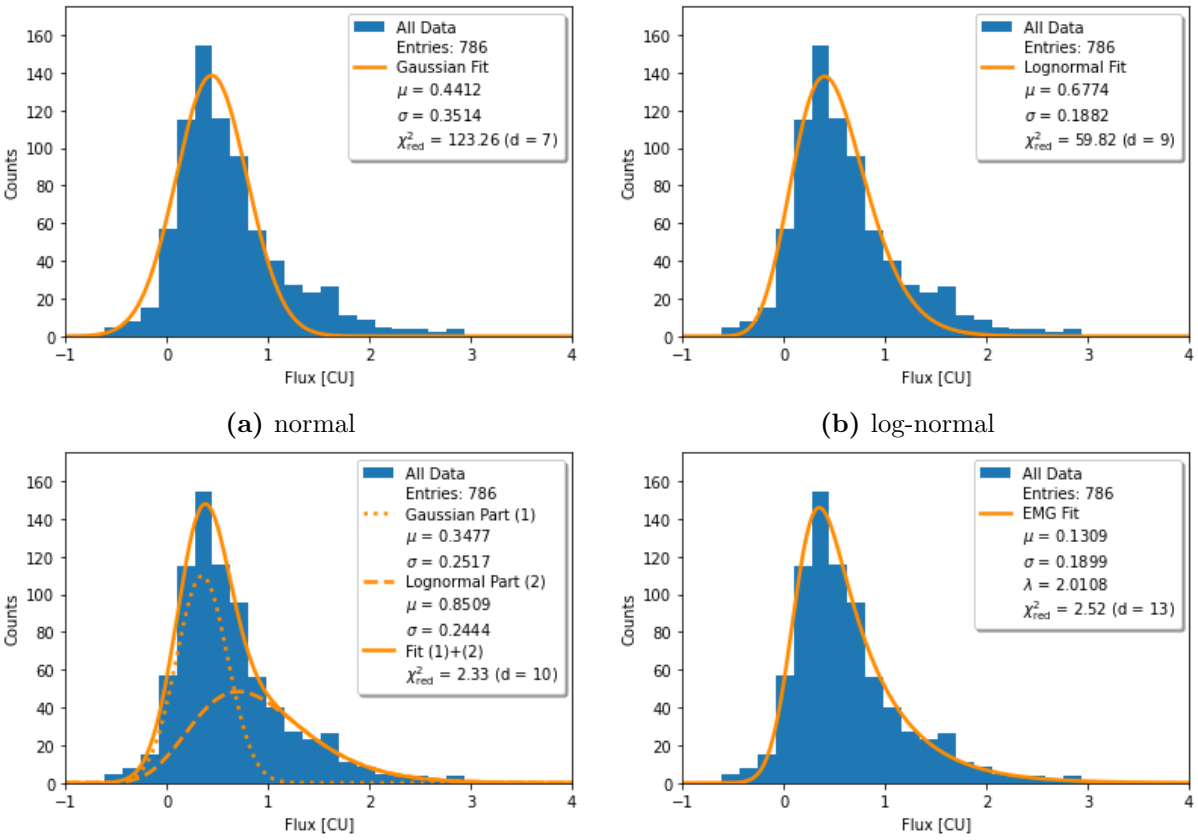

(a) normal **(b)** log-normal

(c) normal + log-normal **(d)** EMG

Figure 2.6.: Distribution of nightly binned fluxes of Mrk 421 as measured by FACT from 2012 to 2019. The flux range of the plots covers only bins that are visible on the y-scale whereby all data is included for the fitting. The respective fit function is indicated by the orange line. The combination of the normal and log-normal distributions shows the smallest χ^2_{red}.

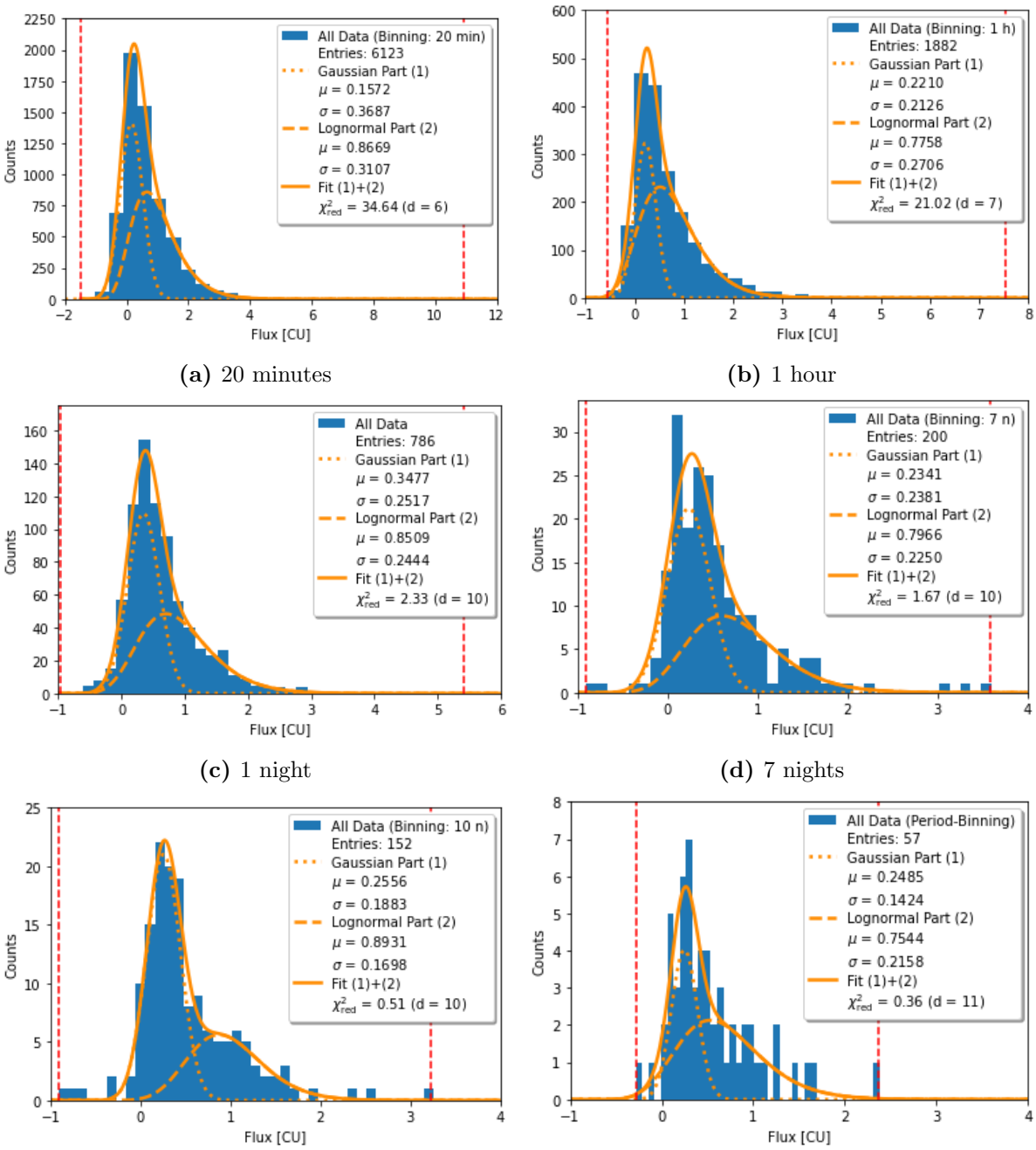

(a) 20 minutes

(b) 1 hour

(c) 1 night

(d) 7 nights

(e) 10 nights

(f) 1 lunar period (≈ 30 nights)

Figure 2.7.: Distributions of fluxes of Mrk 421 on different time scales as measured by FACT from 2012 to 2019. The fit function is indicated respectively by the orange line and the flux range of the data by the red dashed lines. The larger the time binning, the smaller is the mean error (bin width), the total number of histogram entries and the flux range.

2.4.2. Different Time Binnings

So far only the nightly fluxes have been examined and it has been shown that they are best described by the superposition of a normal and a log-normal distribution. Now the distribution is investigated on different time scales for time binnings in the range of 20 minutes to 1 lunar period (see Figure 2.7). In order to present the statistical properties, regular bins with a bin width corresponding to the mean error of the data set are chosen. For all time binnings, the fit consisting of two components is applied whereby one can notice a decrease of χ^2_{red} with larger binning. In Section 2.6, the fit parameters for Mrk 421 and Mrk 501 will be compared with regard to different time scales, whereas this section focusses on the general effects of different time binnings. For larger binnings, the mean error is smaller and therefore the bins are narrower but also the statistics are lower, which can be seen from the total number of histogram entries. For the period binning (see Figure 2.7f), there are only few histogram entries but many bins according to the small mean error and thus the distribution has gaps, which limits its informative value. The flux range decreases with larger time binnings because extreme flux values average out. Accordingly for small time binnings like 20 minutes, the distribution is characterised by a wide flux range, wide bins and high statistics. This confirms that the nightly binning is an appropriate trade-off between a small mean error and enough histogram entries. For this reason, the nightly fluxes are used for further investigation.

2.4.3. Bayesian Binning

The Bayesian binning described in Section 2.3.2 is applied to the nightly fluxes of Mrk 421 in order to extract the significant features of the data. Compared to the regular binning (see Figure 2.6c), the distribution with Bayesian bins (see Figure 2.8a) shows less bins and a dominating peak for low fluxes which makes it difficult to find a suitable fit function. The Gaussian part in Figure 2.8a is almost entirely defined by the one point at the top center of the peak, which is obviously of limited informative value. Apart from that, unequal bins complicate the calculation of the frequency per category for the χ^2-test because the fit function has to be scaled with the bin width. Hence, it is much easier to plot the probability density of the fluxes, which means that the counts for each bin are already normalised by the bin width and total number of entries (see Figure 2.8b). For the Bayesian density plot, the superposition of the normal and log-normal distributions has a significant larger χ^2_{red} than for the regular binning and the number of degrees of freedom is smaller due to the reduced number of bins. The deviation from the fit distribution mainly results from the peak since the area under the fitted curve is much smaller than the area of the bin which is proportional to the frequency in this category.

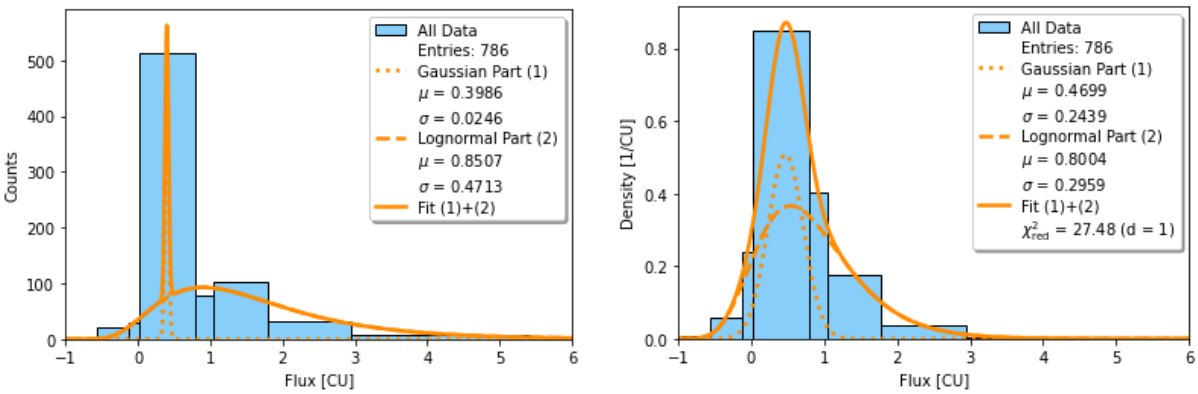

(a) Bayesian counts

(b) Bayesian density

Figure 2.8.: Distribution of nightly binned fluxes of Mrk 421 as measured by FACT from 2012 to 2019. The bins are calculated according to the Bayesian Block algorithm. The respective fit function is indicated by the orange line. For the Bayesian binning, it is necessary to plot the probability density in order to be able to find a meaningful fit function and to calculate the frequencies for the χ^2-test.

It is tested whether another PDF can describe the Bayesian density of the fluxes more suitably (see Figure 2.9). For the normal, log-normal and EMG PDF, standardization can be assumed so that the parameter a can be replaced by a fixed factor, which allows the shift s in the log-normal PDF to be implemented as fit parameter instead of a set value. The EMG fit with $\chi^2_{\text{red}} = 3.98$ (see Figure 2.9d) obviously describes the data best of the four tested distributions.

However, the first bin with negative fluxes is not well included in the fitted EMG PDF so that a data selection cut is performed. The probability distribution of all fluxes is compared with the one of only fluxes with a significance σ of higher than 2 (see Figure 2.10). When removing the fluxes of low significance, the bins for very low fluxes almost disappear but otherwise the distribution remains similar. For the significance cut the log-normal PDF is the most suitable.

The absence of a Gaussian part is consistent with the interpretation of the normal component as steady state emission for which one can only determine an upper limit due to limited sensitivity [4]. In [4], an upper limit of 33% of the flux of the Crab Nebula at TeV energies was determined from combined long-term VHE data of Mrk 421, whereas in [3] a modified method was used to calculate from FACT data a limit of 0.22 CU for the baseline flux. In our case, considering the normal component of the distribution of nightly fluxes as steady state, the upper limit corresponds to the mean value (0.348 ± 0.021) CU from the fit (see Figure 2.6c), which is consistent with the value determined in [4].

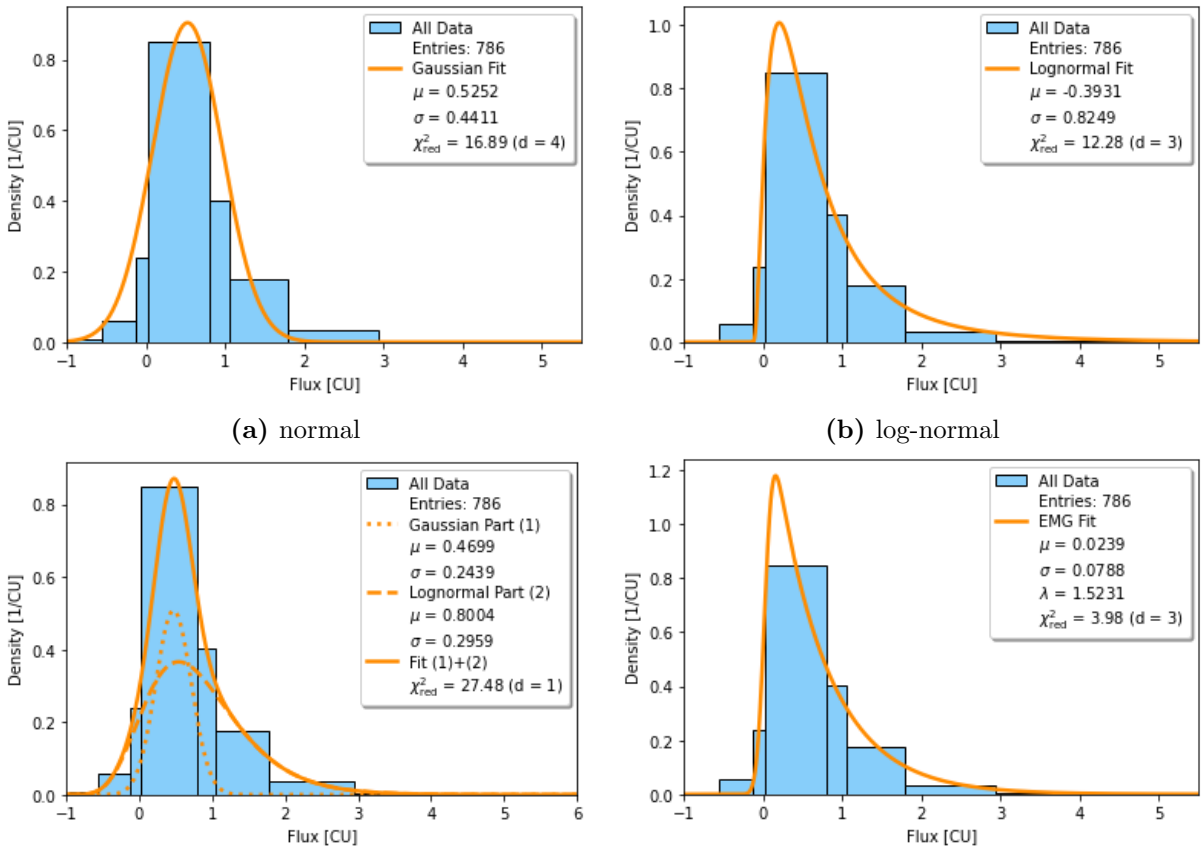

(a) normal **(b)** log-normal

(c) normal + log-normal **(d)** EMG

Figure 2.9.: Probability distribution of nightly binned fluxes of Mrk 421 as measured by FACT from 2012 to 2019. The bins are calculated according to the Bayesian Block algorithm. The respective fit function is indicated by the orange line. The EMG PDF shows the smallest χ^2_{red}.

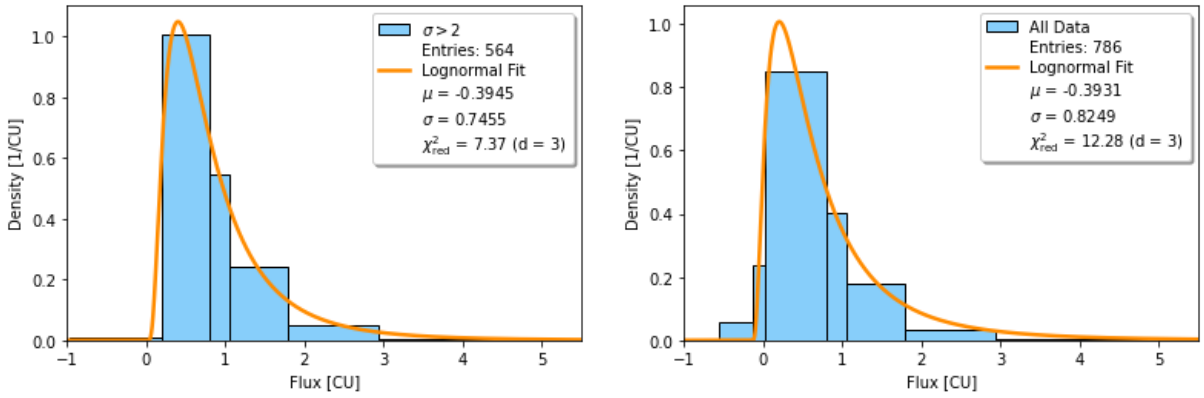

(a) fluxes with $\sigma > 2$ **(b)** all fluxes

Figure 2.10.: Probability distribution of nightly binned fluxes of Mrk 421 as measured by FACT from 2012 to 2019. The bins are calculated according to the Bayesian Block algorithm. The respective fit function is indicated by the orange line. When removing fluxes of low significance σ the bins for very low fluxes almost disappear and the log-normal PDF is most suitable.

2.5. Results Mrk 501

For Mrk 501, the same procedure as for Mrk 421 has been performed to analyse distinct binning effects and the results are presented in the following section. Subsequently, the flux distributions for the individual years are investigated to verify the temporal evolution of Mrk 501.

2.5.1. Binning Effects

As with Mrk 421, the choice of histogram binning influences the resulting distribution of best fit. Figure 2.11a shows that the nightly fluxes of Mrk 501 are only best described by the superposition of a normal and log-normal component for the equal bins but still with a relative large $\chi^2_{\text{red}} = 17.27$. Although the Bayesian binning does not differ as much as for Mrk 421 from the regular binning, the EMG (see Figure 2.11b) and log-normal PDF (see Figure 2.11d) show a significantly smaller χ^2_{red} than the combination fit. Due to subtler binning, the peak of the distribution of Mrk 501 seems to be more characteristic than for Mrk 421. Whereas for the latter, the EMG PDF is most suitable for the Bayesian density plot, for Mrk 501 the log-normal PDF has the smallest $\chi^2_{\text{red}} = 7.13$ (see Figure 2.11d). When removing fluxes of low significance, the log-normal fit with $\chi^2_{\text{red}} = 3.00$ is even more suitable because negative fluxes are reduced (see Figure 2.11c). Apart from that, it can be seen that the Bayesian bins become much wider after the significance cut.
For different time binnings, the same general effects as for Mrk 421 become apparent (see Figure 2.12), which means the larger the time binning, the smaller is the mean error, the total number of histogram entries and the flux range. For Mrk 501, one can furthermore notice that the two components of the fit become more indistinct for smaller time binnings. For the 20-min binning the normal and log-normal parts almost have the same peak positions (see Figure 2.12a) whereas for the period binning they are clearly separated (see Figure 2.12f). It seems like the larger the time scales are, the better is the resolution of two components which possibly describe different flux states. The normal and log-normal components of Mrk 421 and Mrk 501 will be compared in Section 2.6.

2.5.2. Temporal Evolution

In Section 2.2.3, one has already seen from the light curve of Mrk 501 that the flux level decreased significantly over the years (see Figure 2.4b). The source has been regarded as active from 2012 to 2016, whereas the years from 2017 to 2019 have been referred to as low phase. Figure 2.13 shows the distribution of nightly fluxes with its most suitable fit for each year individually. Since for the Bayesian binning the number of categories is often too small to find any fit, regular bin widths have been chosen for the histograms of the individual years.

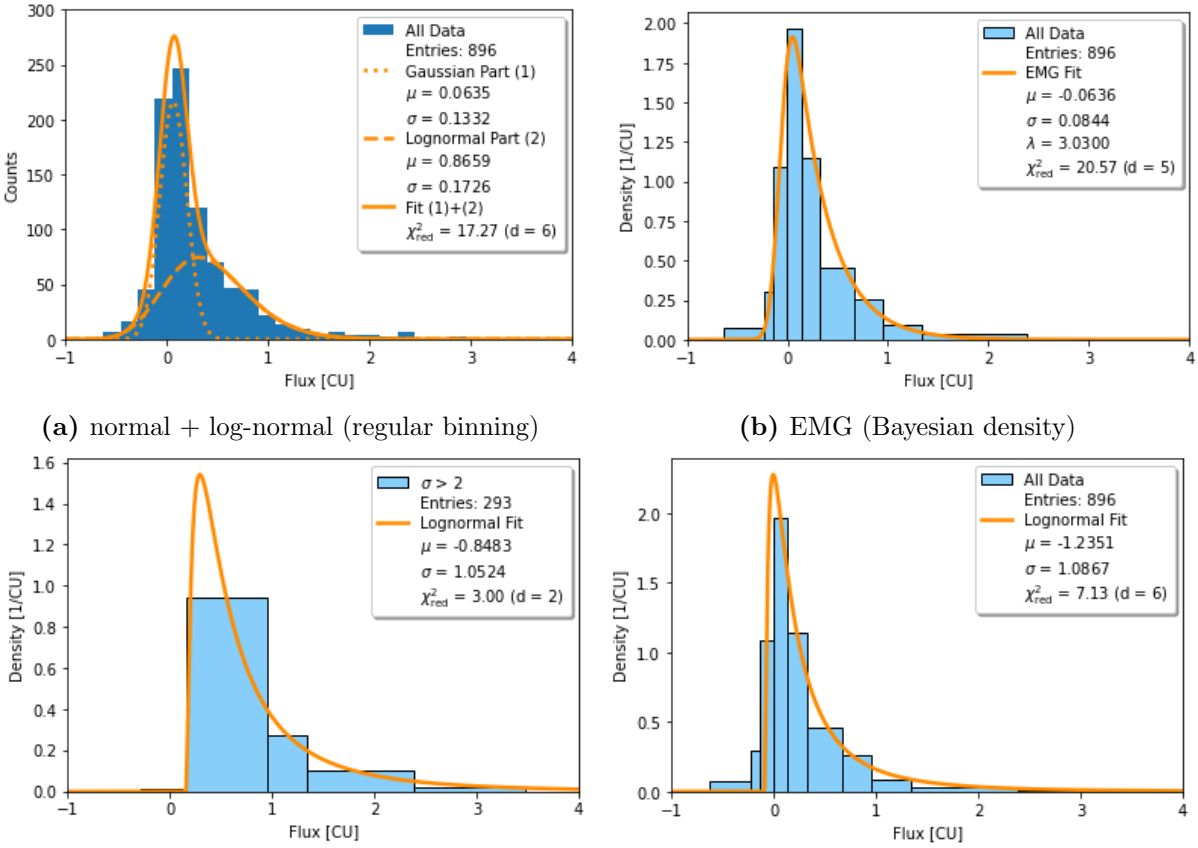

(a) normal + log-normal (regular binning)

(b) EMG (Bayesian density)

(c) log-normal (Bayesian density $\sigma > 2$)

(d) log-normal (Bayesian density)

Figure 2.11.: Distribution of nightly binned fluxes of Mrk 501 as measured by FACT from 2012 to 2019. One very high flux event is not displayed on the flux scale but included for the fitting. The respective fit function is indicated by the orange line. This figure summarizes the most important plots of the analysis of different histogram binnings.

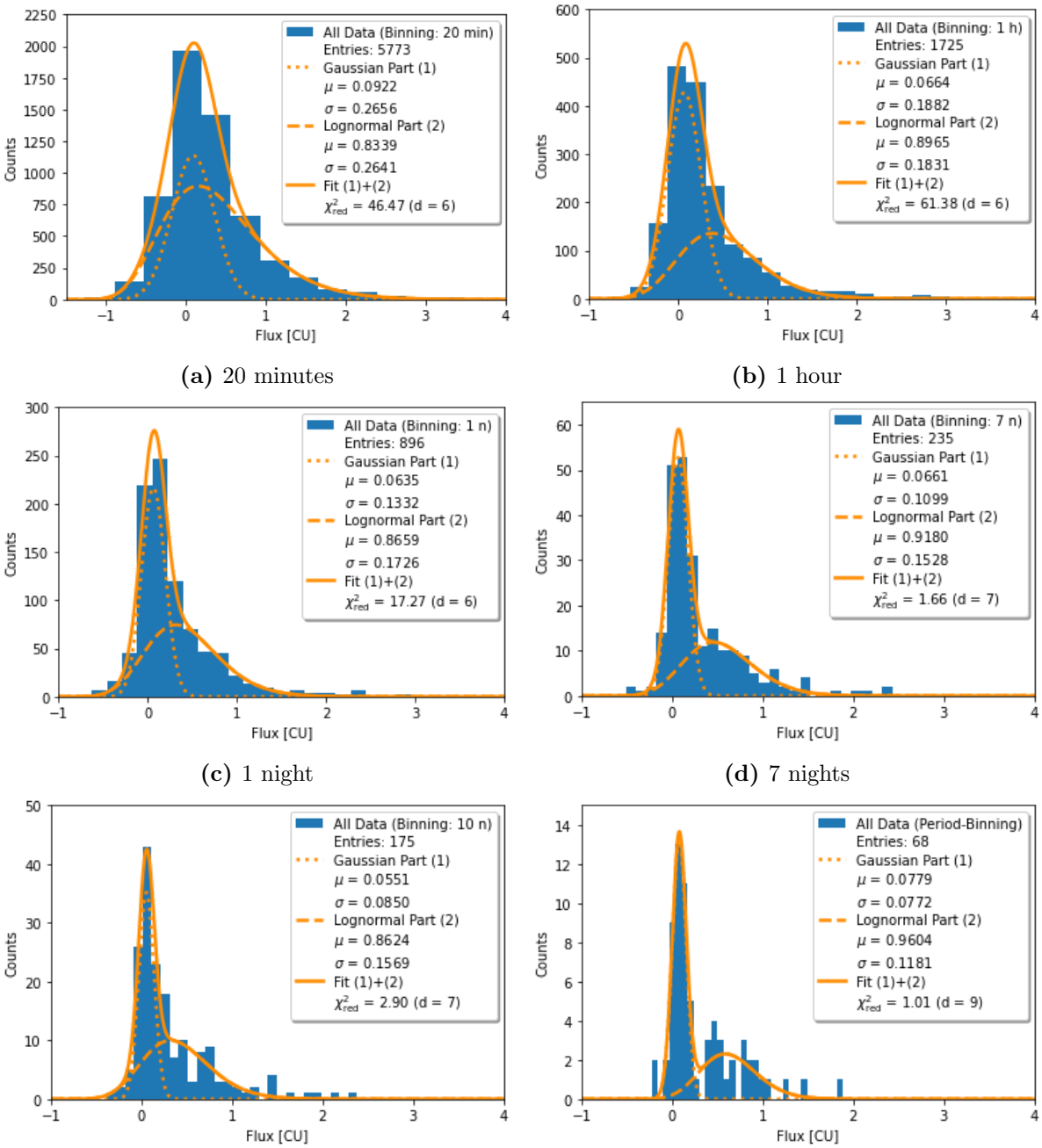

(a) 20 minutes

(b) 1 hour

(c) 1 night

(d) 7 nights

(e) 10 nights

(f) 1 lunar period (≈ 30 nights)

Figure 2.12.: Distributions of fluxes of Mrk 501 on different time scales as measured by FACT from 2012 to 2019. The flux range of the plots covers only bins that are visible on the y-scale whereby all data is included for the fitting. The fit function is indicated respectively by the orange line. The larger the time binning, the better is the resolution of the two fit components.

In 2012, FACT has started monitoring the source not at the beginning of the observation season, which is why the number of histogram entries is lower than for the other years. Another reason why the EMG fit for 2012 might be of less informative value is the presence of one very high flux event which is included in the fitting (see Figure 2.13a). However, from 2013 on, one can observe an evolution from a log-normal to a normal distribution. For 2015 and 2016, both components are present, which might indicate a gradual phase transition (see Figure 2.13d and 2.13e). The distribution of 2017 seems almost Gaussian but the log-normal fit with little positive skewness shows the smaller χ^2_{red} (see Figure 2.13f). The distributions of 2018 and 2019 could theoretically also be described by EMG or log-normal PDFs but with parameters that make them look like Gaussians so in these cases it is more reasonable to fit normal distributions (see Figure 2.13g and 2.13h).
The flux distributions obviously reflect the transition from an active to a steady state. The latter is expressed by a Gaussian, whereas the active state is possibly described by a log-normal distribution.
When combining the fluxes of the active years from 2012 to 2016, their distribution shows the smallest χ^2_{red} for the EMG fit (see Figure 2.14a). This shows that the active phase does not necessarily have to exhibit a log-normal behaviour but rather the feature of highly positive skewness which results from several flaring events. In contrast, from 2017 to 2019 the flux level was almost zero so that the source was below the detection threshold in individual nights. The significance of the signal was only $3.72\,\sigma$[7] during this observation period, whereas from 2012 to 2016 the significance was $66.65\,\sigma$[8]. It seems like the blazar has switched off since 2017 or is at least found in an extreme quiescent state. According to the fitted normal distribution in Figure 2.14b, the standard deviation $\sigma = 0.13\,\text{CU}$ is similar to the width of the distribution of the non-detected source 1H0323+342 and therefore primarily reflects the statistical and systematic errors of the flux measurement. The mean value is $\mu = (0.0357 \pm 0.0026)\,\text{CU}$ which can be interpreted as the upper limit for the baseline flux. For comparison, the limit according to the normal component of the distribution of nightly fluxes over the whole observation period is $\mu = (0.0635 \pm 0.0028)\,\text{CU}$ (see Figure 2.11a). In [3], an even lower limit of 2% of the flux of the Crab Nebula at TeV energies was determined from the low state of Mrk 501.

[7]FACT Database Explorer, Mrk 501 (2017-19): `https://www.fact-project.org/dch/db_explorer.php?short=11384`, 18.02.2021
[8]FACT Database Explorer, Mrk 501 (2012-16): `https://www.fact-project.org/dch/db_explorer.php?short=11386`, 18.02.2021

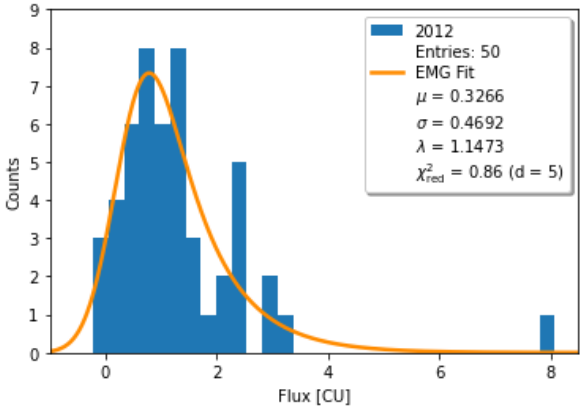

(a) 2012 - EMG

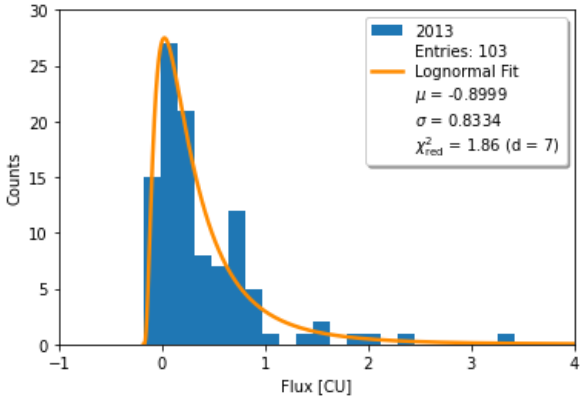

(b) 2013 - log-normal

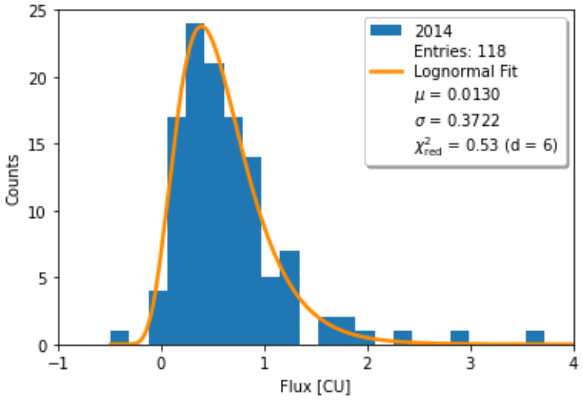

(c) 2014 - log-normal

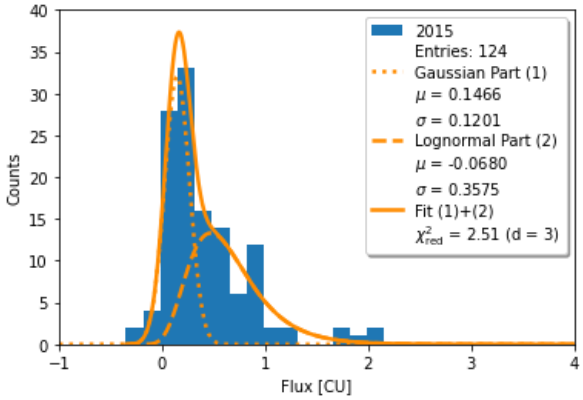

(d) 2015 - normal + log-normal

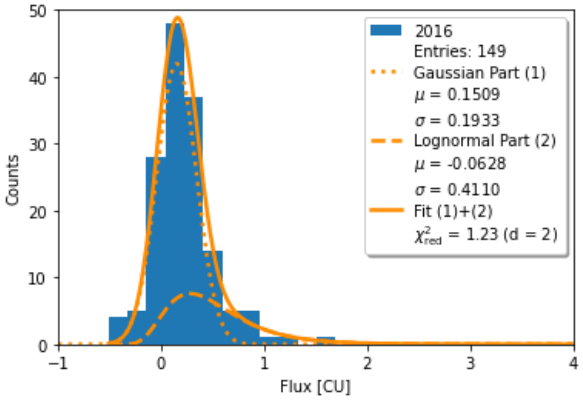

(e) 2016 - normal + log-normal

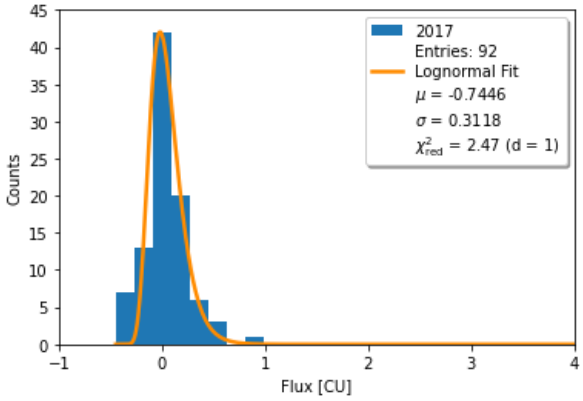

(f) 2017 - log-normal

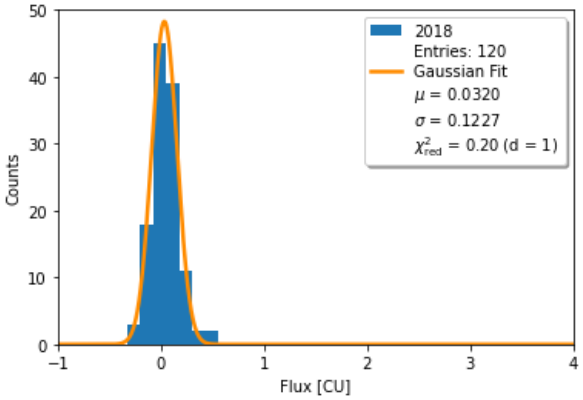

(g) 2018 - normal

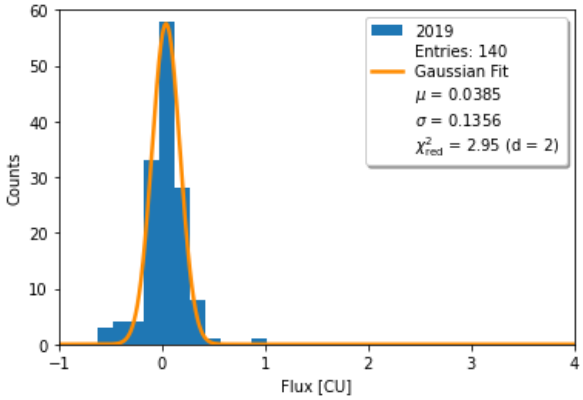

(h) 2019 - normal

Figure 2.13.: Distributions of nightly binned fluxes of Mrk 501 for individual years as measured by FACT. The most suitable fit is indicated by the orange line.

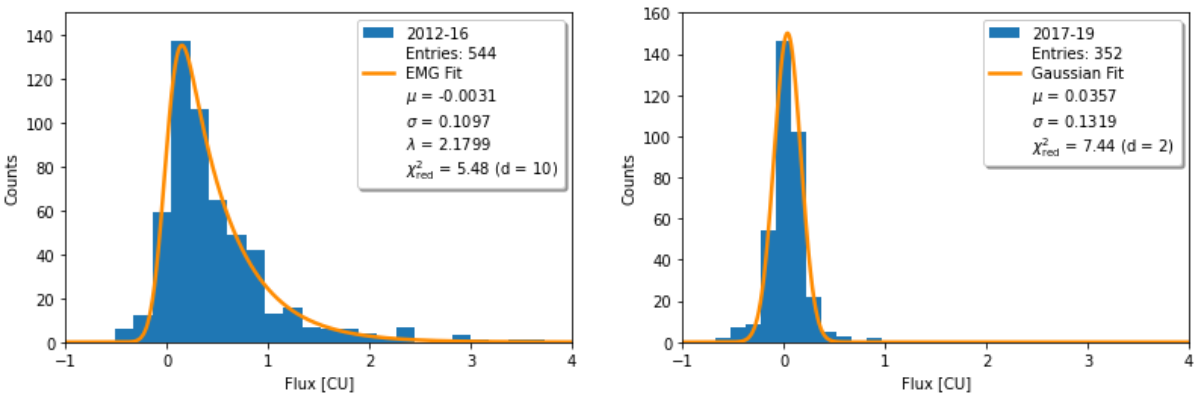

(a) active phase (2012-2016) - EMG **(b)** low phase (2017-2019) - normal

Figure 2.14.: Distributions of nightly binned fluxes of Mrk 421 as measured by FACT. One very high flux event is not displayed on the flux scale of the active phase but is included for the fitting. The respective fit function is indicated by the orange line.

2.6. Comparison of Mrk 421 and Mrk 501

In order to compare the flux distributions of Mrk 421 and Mrk 501 on different time scales (see Figure 2.7 and 2.12), the respective fit parameter μ is plotted as a function of the time binning both for the normal and log-normal component (see Figure 2.15). The parameter σ is plotted as error bars of μ since it represents the width of the distribution and thus can be interpreted as the error of the mean value μ.

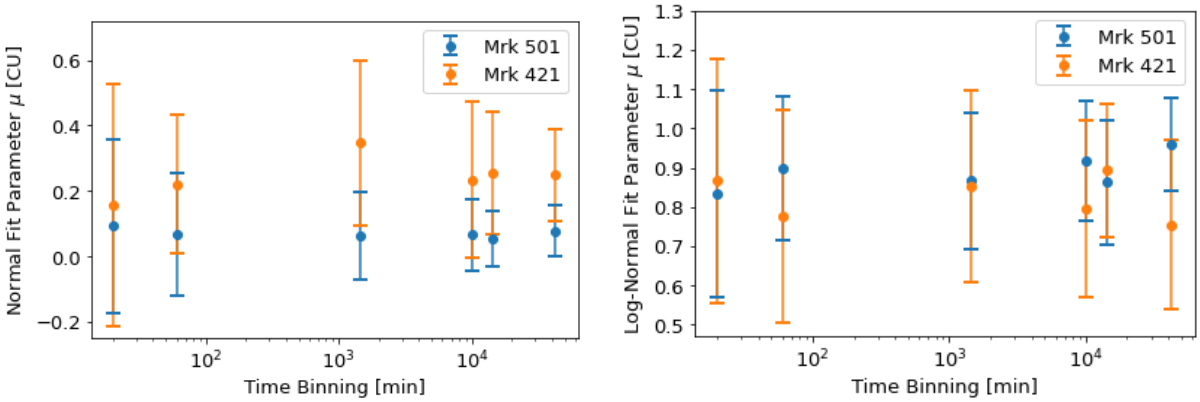

(a) normal component **(b)** log-normal component

Figure 2.15.: Comparison of the fit parameters of Mrk 421 (see Figure 2.7) and Mrk 501 (see Figure 2.12) on different time scales. For both components σ is plotted as error bars of μ. The mean value μ of the normal part of Mrk 501 is lower than for Mrk 421. For the log-normal component one can not notice a consistent tendency.

For the normal component, one can clearly see that the mean value μ of Mrk 501 is lower and almost constant for different time binnings (see Figure 2.15a), which indicates that Mrk 501 has the lower ground state independently of the time scales. At least for Mrk 501, the parameter σ decreases with larger time binnings, which is due to the fact that there are less fluctuations on larger time scales.
For the log-normal component, one can not notice a consistent tendency. Yet, for both components the respective value of σ of Mrk 421 is higher than for Mrk 501 on all time scales. From this one can conclude that Mrk 421 is the more variable source and thus has a wider distribution, which also can be seen in direct comparison of the flux distributions (see Figure 2.16).

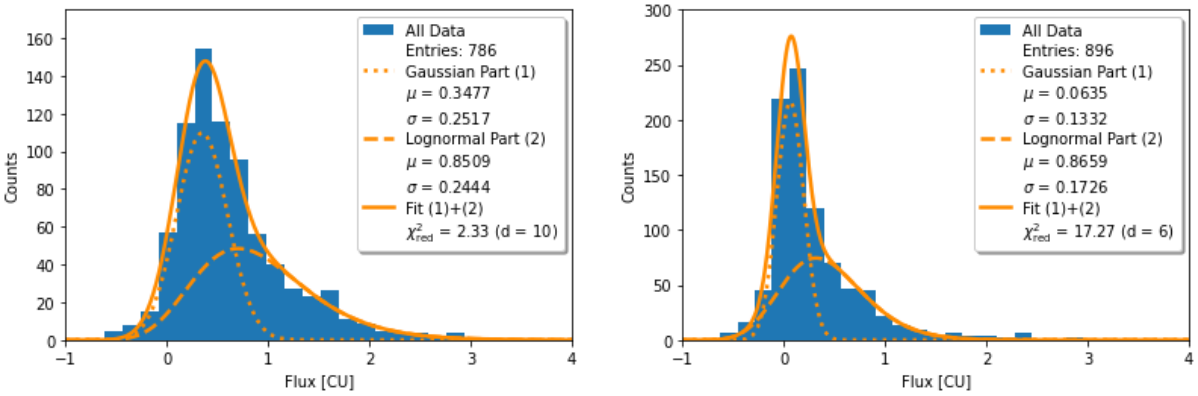

(a) Mrk 421 **(b)** Mrk 501

Figure 2.16.: Comparison of the distributions of nightly binned fluxes of Mrk 421 and Mrk 501 as measured by FACT from 2012 to 2019. The flux range of the plots covers only bins that are visible on the y-scale whereby all data is included for the fitting. The fit function is indicated by the orange line. Mrk 421 has a wider distribution than Mrk 501 and is thus more variable. The normal component of Mrk 501 has its mean value closer to zero, which means that the ground state is lower than for Mrk 421.

3. Conclusion

This work was motivated by probing the existence of distinct flux states in blazars, and in particular their imprint on flux distributions in the VHE regime. Ambiguous physical interpretations of normal and log-normal flux distributions were discussed. The distributions of nightly fluxes as measured by FACT from 2012 to 2019 were examined with respect to their underlying shape. Four different distribution functions were tested on each data set respectively and evaluated according to their χ^2_{red}.

It was demonstrated that the presence of normal and log-normal components in the flux distributions of Mrk 421 and Mrk 501 is not a significant feature since it could only be determined for the regular but not for the Bayesian histogram binning. The latter is used to find the optimal binning of the data in an unbiased way but due to the reduced number of bins, the fitting can be more difficult. The Bayesian density distribution is best described by a EMG PDF for Mrk 421 and by a log-normal PDF for Mrk 501 and not by the superposition of a normal and log-normal component. The data selection cut with respect to significance ($\sigma > 2$) showed that both for Mrk 421 and Mrk 501 the log-normal PDF is then most suitable. The fact that the histogram binning can influence the results significantly sounds a note of caution when prematurely deriving physical mechanisms from the flux distributions.

The time binning of the light curves affects the mean error, the total number of histogram entries and the flux range of the data. It became apparent that the nightly binning is an appropriate trade-off between a small mean error and enough histogram entries.

The temporal evolution of Mrk 501 from an active to a quiescent state is reflected in its flux distributions by the transition from a log-normal to a normal one, which was shown by investigating the distributions of the individual years. The fact that the active phase combining the years from 2012 to 2016 is best described by a EMG distribution leads to the conclusion that any positively skewed distribution function can potentially describe active flux states. Contrary to widespread assumptions, this shows that log-normalcy is not necessarily special. The low phase of Mrk 501 from 2017 to 2019 is expressed by a Gaussian flux distribution with a mean value $\mu = (0.0357 \pm 0.0026)\,\mathrm{CU}$ which can be interpreted as upper limit for the baseline flux [3]. The source could barely be detected by FACT during this period and thus the standard deviation $\sigma = 0.13\,\mathrm{CU}$ primarily reflects the statistical and systematic errors of the flux measurement.

Generally, the flux distributions of Mrk 421 and Mrk 501 exhibit similar properties. The comparison of fit parameters on different time scales revealed that Mrk 501 has the lower ground state, whereas Mrk 421 is more variable. While the upper limits for the steady state of both sources are higher than calculated in [3], the limit for Mrk 421 of 35% of the flux of the Crab Nebula at TeV energies is consistent with the one determined in [4].

Bibliography

[1] R. D. Blandford and A. Königl, "Relativistic jets as compact radio sources," *The Astrophysical Journal*, vol. 232, pp. 34–48, 1979.

[2] J. D. Scargle, "Studies in astronomical time series analysis: Vii. an enquiry concerning non-linearity, the rms-mean flux relation, and log-normal flux distributions," *The Astrophysical Journal*, vol. 895, no. 2, p. 90, 2020.

[3] D. Dorner, A. Arbet-Engels, D. Baack, M. Balbo, A. Biland, M. Blank *et al.*, "Flux states of active galactic nuclei," *Galaxies*, vol. 7, no. 2, p. 57, 2019.

[4] M. Tluczykont, E. Bernardini, K. Satalecka, R. Clavero, M. Shayduk, and O. Kalekin, "Long-term lightcurves from combined unified very high energy γ -ray data," *Astronomy & Astrophysics*, vol. 524, p. A48, 2010.

[5] V. Beckmann and C. R. Shrader, *Active galactic nuclei*, ser. Physics textbook. Weinheim and Chichester: Wiley-VCH, 2012.

[6] T. C. Weekes, *Very high energy gamma-ray astronomy*, ser. Series in astronomy and astrophysics. Bristol: Inst. of Physics Publ, 2003.

[7] L. Duband, "Space cryocooler developments," *Physics Procedia*, vol. 67, pp. 1–10, 2015.

[8] T. M. Shaffer, E. C. Pratt, and J. Grimm, "Utilizing the power of cerenkov light with nanotechnology," *Nature nanotechnology*, vol. 12, no. 2, pp. 106–117, 2017.

[9] A. A. Abdo, M. Ackermann, M. Ajello, L. Baldini, J. Ballet, G. Barbiellini *et al.*, "Fermi large area telescope observations of markarian 421: The missing piece of its spectral energy distribution," *The Astrophysical Journal*, vol. 736, no. 2, p. 131, 2011.

[10] K. Katarzyński, G. Ghisellini, F. Tavecchio, L. Maraschi, G. Fossati, and A. Mastichiadis, "Correlation between the tev and x-ray emission in high-energy peaked bl lac objects," *Astronomy & Astrophysics*, vol. 433, no. 2, pp. 479–496, 2005.

[11] A. R. Choudhuri, *Astrophysics for physicists*. Cambridge: Cambridge Univ. Press, 2010.

[12] N. I. Shakura and R. A. Sunyaev, "A theory of the instability of disk accretion on to black holes and the variability of binary x-ray sources, galactic nuclei and quasars," *Mon. Not. R. Astron. Soc.*, vol. 175, pp. 613–632, 1976.

[13] P. Uttley, I. M. McHardy, and S. Vaughan, "Non-linear x-ray variability in x-ray binaries and active galaxies," *Monthly Notices of the Royal Astronomical Society*, vol. 359, no. 1, pp. 345–362, 2005.

[14] B. Giebels and B. Degrange, "Lognormal variability in bl lacertae," *Astronomy & Astrophysics*, vol. 503, no. 3, pp. 797–799, 2009.

[15] Y. E. Lyubarskii, "Flicker noise in accretion discs," *Mon. Not. R. Astron. Soc.*, vol. 292, pp. 679–685, 1997.

[16] H. Anderhub, M. Backes, A. Biland, V. Boccone, I. Braun, T. Bretz *et al.*, "Design and operation of fact – the first g-apd cherenkov telescope," *Journal of Instrumentation*, vol. 8, no. 06, pp. P06 008–P06 008, 2013.

[17] D. Dorner, M. L. Ahnen, M. Bergmann, A. Biland, M. Balbo, T. Bretz *et al.*, "Fact - monitoring blazars at very high energies," *5th Fermi Symposium*, pp. 20–24, 2014.

[18] A. Biland, T. Bretz, J. Buß, V. Commichau, L. Djambazov, D. Dorner *et al.*, "Calibration and performance of the photon sensor response of fact — the first g-apd cherenkov telescope," *Journal of Instrumentation*, vol. 9, no. 10, pp. P10 012–P10 012, 2014.

[19] T. Bretz, "Zenith angle dependence of the cosmic ray rate as measured with imaging air-cherenkov telescopes," *Astroparticle Physics*, vol. 111, pp. 72–86, 2019.

[20] D. Hildebrand, M. L. Ahnen, M. Balbo, A. Biland, T. Bretz, J. Buss *et al.*, "Using charged cosmic ray particles to monitor the data quality of fact," in *Proceedings of 35th International Cosmic Ray Conference — PoS(ICRC2017)*, I. H. Park, H. S. Lee, S. Oh, and Y.-S. Kwak, Eds. Trieste, Italy: Sissa Medialab, 10-20 July, 2017, p. 779.

[21] M. Mahlke, T. Bretz, J. Adam, L. M. Ahnen, D. Baack, M. Balbo *et al.*, "Fact - searching for periodicity in five-year light-curves of active galactic nuclei," in *Proceedings of 35th International Cosmic Ray Conference — PoS(ICRC2017)*, I. H. Park, H. S. Lee, S. Oh, and Y.-S. Kwak, Eds. Trieste, Italy: Sissa Medialab, 10-20 July, 2017, p. 612.

[22] J. D. Scargle, J. P. Norris, B. Jackson, and J. Chiang, "Studies in astronomical time series analysis. vi. bayesian block representations," *The Astrophysical Journal*, vol. 764, no. 2, p. 167, 2013.

A. Appendix

A.1. Overview of Fit Parameters

Plot	Crab	Crab (Zd > 30°, Th < 350)	1H0323+342	1H0323+342 (Zd > 30°, Th < 350)
Δx [CU]	0.21	0.18	0.15	0.12
μ [CU]	0.9249±0.0049	0.928±0.012	0.0063±0.0045	0.0048±0.0023
σ [CU]	0.2033±0.0049	0.166±0.011	0.1391±0.0043	0.1243±0.0023
a	238.9±5.0	160.4±9.6	166.0±4.5	118.5±1.9
χ^2_{red}	7.80	7.58	4.36	0.92
d	3	2	2	2

Table A.1.: Normal fits

Plot	Mrk 421	Mrk 421 (Bay.)	Mrk 501 (2018)	Mrk 501 (2019)	Mrk 501 (2017-2019)
Δx [CU]	0.18	-	0.13	0.15	0.15
μ [CU]	0.441±0.018	0.525±0.057	0.0320±0.0031	0.0385±0.0061	0.0357±0.0026
σ [CU]	0.351±0.018	0.441±0.048	0.1227±0.0031	0.1356±0.0059	0.1319±0.0025
a	138.5±6.1	-	48.3±1.1	57.5±2.2	150.1±2.4
χ^2_{red}	123.26	16.89	0.20	2.95	7.44
d	7	4	1	2	2

Table A.2.: Normal fits

Plot	Mrk 421 (Bay.)	Mrk 421 (Bay. $\sigma > 2$)	Mrk 501 (Bay.)	Mrk 501 (Bay. $\sigma > 2$)
μ [CU]	-0.393±0.090	-0.395±0.034	-1.24±0.12	-0.85±0.11
σ [CU]	0.825±0.062	0.745±0.046	1.09±0.15	1.05±0.17
s [CU]	-0.137±0.027	0.017±0.038	-0.094±0.017	0.154±0.067
χ^2_{red}	12.28	7.37	7.13	3.00
d	3	3	6	2

Table A.3.: Log-normal fits (Bayesian density)

Plot	Mrk 421	Mrk 501 (2013)	Mrk 501 (2014)	Mrk 501 (2017)
Δx [CU]	0.18	0.16	0.18	0.18
μ [CU]	0.6774±0.0072	-0.900±0.081	0.013±0.017	-0.745±0.033
σ [CU]	0.1882±0.0071	0.833±0.051	0.372±0.016	0.312±0.024
a	50.2±1.7	7.90±0.48	22.48±0.82	19.0±1.4
s [CU]	-1.5	-0.18	-0.49	-0.45
χ^2_{red}	59.82	1.86	0.53	2.47
d	9	7	6	1

Table A.4.: Log-normal fits

Plot	Mrk 421	Mrk 421 (Bay.)	Mrk 501 (Bay.)	Mrk 501 (2012)	Mrk 501 (2012-16)
Δx [CU]	0.18	-	-	0.28	0.18
μ [CU]	0.1309±0.0097	0.024±0.019	-0.0636±0.0092	0.33±0.12	-0.0031±0.0064
σ [CU]	0.190±0.010	1.52±0.11	0.084±0.013	0.47±0.13	0.1097±0.0084
λ [1/CU]	2.01±0.10	0.079±0.023	3.03±0.24	1.15±0.34	2.180±0.096
a	134.4±2.7	-	-	14.0±1.3	96.0±1.9
χ^2_{red}	2.52	3.98	20.57	0.86	5.48
d	13	3	5	5	10

Table A.5.: EMG fits

Plot	Mrk 421 (Bay.)	Mrk 501 (2015)	Mrk 501 (2016)
Δx [CU]	-	0.17	0.18
μ_{gauss} [CU]	0.470±0.011	0.147±0.021	0.151±0.030
σ_{gauss} [CU]	0.244±0.012	0.120±0.022	0.193±0.011
a_{gauss}	0.507±0.031	32.1±9.3	42±12
$\mu_{\log}$ [CU]	0.800±0.014	-0.07±0.15	-0.06±0.41
$\sigma_{\log}$ [CU]	0.2959±0.0093	0.36±0.15	0.41±0.24
$a_{\log}$	0.780±0.059	11.7±1.8	6.5±4.6
s [CU]	-1.5	-0.35	-0.51
χ^2_{red}	27.48	2.51	1.23
d	1	3	2

Table A.6.: Normal + log-normal fits

Binning	20 min	1 h	1 n	7 n	10 n	1 period
Δx [CU]	0.47	0.27	0.18	0.12	0.11	0.07
μ_{gauss} [CU]	0.1572±0.0050	0.2210±0.0095	0.348±0.021	0.234±0.042	0.256±0.015	0.249±0.028
σ_{gauss} [CU]	0.3687±0.0041	0.213±0.016	0.252±0.036	0.238±0.098	0.188±0.012	0.142±0.040
a_{gauss}	1409±127	323±27	110±36	21±30	21.0±1.6	4.0±1.1
$\mu_{\log}$ [CU]	0.867±0.029	0.776±0.026	0.85±0.13	0.80±0.53	0.893±0.043	0.754±0.092
$\sigma_{\log}$ [CU]	0.311±0.015	0.271±0.011	0.244±0.059	0.23±0.27	0.170±0.041	0.216±0.051
$a_{\log}$	1949±78	485±27	110±29	19±19	13.5±1.3	4.4±1.1
s [CU]	-1.5	-1.5	-1.5	-1.5	-1.5	-1.5
χ^2_{red}	34.64	21.02	2.33	1.67	0.51	0.36
d	6	7	10	10	10	11

Table A.7.: Mrk 421 - Different time binnings (normal + log-normal fits)

Binning	20 min	1 h	1 n	7 n	10 n	1 period
Δx [CU]	0.37	0.21	0.17	0.11	0.10	0.07
μ_{gauss} [CU]	0.0922±0.0065	0.0664±0.0047	0.0635±0.0028	0.0661±0.0048	0.0551±0.0070	0.0779±0.0060
σ_{gauss} [CU]	0.2656±0.0088	0.1882±0.0090	0.1332±0.0052	0.1099±0.0080	0.0850±0.0084	0.0772±0.0066
a_{gauss}	1136±54	427±32	216.2±6.5	52.7±3.7	35.2±3.0	13.25±0.93
$\mu_{\log}$ [CU]	0.8339±0.0092	0.896±0.034	0.866±0.013	0.918±0.036	0.862±0.033	0.960±0.029
$\sigma_{\log}$ [CU]	0.2641±0.0045	0.183±0.016	0.1726±0.0065	0.153±0.029	0.157±0.024	0.118±0.034
$a_{\log}$	1990±106	327±33	174.3±9.7	29.4±2.8	23.3±3.2	6.0±1.1
s [CU]	-1.99	-1.99	-1.99	-1.99	-1.99	-1.99
χ^2_{red}	46.47	61.38	17.27	1.66	2.90	1.01
d	6	6	6	7	7	9

Table A.8.: Mrk 501 - Different time binnings (normal + log-normal fits)

A.2. Implementation of the chi-squared Test in Python

```python
#example script for plotting the flux distribution with normal+log-normal as fit function

import numpy as np
import pandas as pd
import matplotlib.pyplot as plt
import matplotlib.patches as mpatches
from scipy.optimize import curve_fit
from scipy import stats
from scipy import integrate


data = pd.read_excel(...)

xmin = -1
xmax = 6
entries = np.shape(data['corrected_flux[CU]'])
shift = -1.5

def norm(x,d,e,f):
    return d * np.exp(-1.0 * (x - e)**2 / (2 * f**2))

def lognorm(x,a,b,c):
    return a * np.exp(-1.0 * (np.log(x - shift) - b)**2 / (2 * c**2))/(x-shift)

def fit_function(x,a,b,c,d,e,f):
    return lognorm(x,a,b,c) + norm(x,d,e,f)


err_mean = np.mean(data['corrected_flux_error[CU]'])
print(err_mean)
bins = [data['corrected_flux[CU]'].min()]
i=0
while bins[i] <= data['corrected_flux[CU]'].max():
    bins.append(bins[i] + err_mean)
    i = i+1

(n, bins, patches) = plt.hist(data['corrected_flux[CU]'], bins = bins)

binscenters = np.array([0.5 * (bins[i] + bins[i+1]) for i in range(len(bins)-1)])

(popt, pcov) = curve_fit(fit_function, xdata=binscenters, ydata=n,
                         p0=[10, -1.1, 0.937, 100,0.210,0.224])
print(popt)
perr = np.sqrt(np.diag(pcov))
print(perr)

xspace = np.linspace(xmin, xmax, 100000)
fit = plt.plot(xspace, fit_function(xspace, *popt), color='darkorange', linewidth=2.5)
gauss = plt.plot(xspace, norm(xspace, *popt[3:6]), color='darkorange', linewidth=2.5,
                 linestyle=':')
log = plt.plot(xspace, lognorm(xspace, *popt[0:3]), color='darkorange', linewidth=2.5,
               linestyle='--')

#implementation chi-squared test:
tails = [0] #expected frequencies at the tails of the distribution
f_exp = [] #expected frequencies per category
f_obs = [] #observed frequencies per category
df = lambda x: (fit_function(x,*popt)/err_mean) #expected frequency density function
den = n/err_mean #observed frequency density

#combination of categories at the tails until the expected frequency is at least 5
```

```
for i in range(0,len(bins)):
    if integrate.quad(df, shift, bins[i])[0] >= 5:
        tails[0] = integrate.quad(df, shift, bins[i])[0]
        start = i
        break

for i in range(0,len(bins)):
    if integrate.quad(df, bins[i], np.inf)[0] < 5:
        tails.append(integrate.quad(df, bins[i-1], np.inf)[0])
        end = i-1
        break

#calculation of the expected frequencies per category
for i in range(start,end):
    f_exp.append(integrate.quad(df, shift, bins[i+1])[0]-
                 integrate.quad(df, shift, bins[i])[0])

f_exp =  np.hstack((tails[0], f_exp, tails[1]))

#calculation of the observed frequencies per category
summe1 = 0
summe2 = 0
for i in range (0,start):
    summe1 = summe1 + abs(bins[i]-bins[i+1])*den[i]
for i in range (end,len(bins)-1):
    summe2 = summe2 + abs(bins[i]-bins[i+1])*den[i]
f_obs.append(summe1)
for i in range (start,end):
   f_obs.append(abs(bins[i]-bins[i+1])*den[i])
f_obs.append(summe2)

#calculation of chi-square
(chisq,p) = stats.chisquare(f_obs, f_exp, ddof=6)
#number of degrees of freedom = number of categories - number of fit parameters:
d = len(f_exp)-6
print(chisq/d) #reduced chi-square


plt.xlim(xmin, xmax)
plt.ylim(0, 175)
plt.xlabel(r'Flux [CU]')
plt.ylabel(r'Counts')

empty_patch = mpatches.Patch(color='none')
plt.legend((patches[0],empty_patch, gauss[0], empty_patch, empty_patch, log[0],
            empty_patch, empty_patch, fit[0],empty_patch),
           ('All Data','Entries: %.0f'%entries[0], 'Gaussian Part (1)',
            '$\mu$ = %.4f'%popt[4],'$\sigma$ = %.4f' %popt[5], 'Lognormal Part (2)',
            '$\mu$ = %.4f'%popt[1],'$\sigma$ = %.4f' %popt[2], 'Fit (1)+(2)',
            '$\chi^{2}_{\mathrm{red}}$ = %.2f (d = %.0f)'%(chisq/d,d)),
           loc=1, shadow = True, labelspacing = 0.3)
plt.show()
```

Acknowledgements

I would like to thank Prof. Dr. Karl Mannheim for providing insights into the work done at his chair and for giving me the opportunity to contribute to the research in astronomy which I have always been interested in.
I am very grateful for being part of the Gamma-Group of Daniela Dorner. Although I have met Dani and Co. only one time in person, I got to know them all quite well during our weekly Zoom meetings. Despite these difficult times of home office, we managed to exchange ideas and support each other. Especially, I want to thank Daniela Dorner and Karl Mannheim for being so flexible concerning the preparation of this thesis, which was continued during my four-month stay at CERN.
I was also lucky to have Paul Ray Burd and Sarah Wagner who gave me lots of helpful advice in terms of flux distributions and programming.
Apart from that, I thank the FACT collaboration for kindly providing their data.
Finally, I want to thank my family and friends for their unconditional support in many ways. Special thanks go to Nora who was not only my expert for English language skills but also gives me honest advice in every situation. Above all, I am more than grateful to have Carsten by my side. He gives me the moral support and inspiration I need.

Erklärung

Hiermit erkläre ich, dass ich die vorliegende Arbeit selbständig verfasst und keine anderen als die angegebenen Quellen und Hilfsmittel verwendet habe. Die Arbeit wurde keiner anderen Prüfungsbehörde unter Erlangung eines akademischen Grades vorgelegt.

Würzburg, den 28.02.2021 ..... L. Eisenberger ..... (Unterschrift)

Laura Eisenberger